J. Non-Newtonian Fluid Mech. 162 (2009) 1–20

Contents lists available at ScienceDirect

Journal of Non-Newtonian Fluid Mechanics

journal homepage: www.elsevier.com/locate/jnnfm

Numerical simulation of viscoelastic fluids in cross-slot devices

B. Puangkird[a,b], F. Belblidia[a], M.F. Webster[a,*]

[a] Institute of Non-Newtonian Fluid Mechanics, School of Engineering, Swansea University, Singleton Park, Swansea SA2 8PP, UK
[b] King Mongkut's Institute of Technology Ladkrabang, Bangkok 10520, Thailand

ARTICLE INFO

Article history:
Received 15 September 2008
Received in revised form 30 April 2009
Accepted 4 May 2009

Keywords:
Constitutive models
Cross-slot flow
Planar elongational flow
Viscoelastic

ABSTRACT

Cross-slot flow for viscoelastic fluids is investigated through various numerical algorithms, demonstrating the effectiveness of such devices to study constitutive models and their resulting rheological properties. Here, the steady problem manifests the long-time exposure to significant extension. Solutions are compared and contrasted for a range of rheological models of varying shear and extensional response, including phenomenologically based models from network-theory of Oldroyd/Phan-Thien–Tanner class, and also kinetic-theory based forms of FENE-CR and pom-pom. Matching rheological fluid characteristics are sought across various models through peak extensional viscosity and Trouton ratio. Using the Oldroyd-B model and for the more solvent-dominated fluid, deformation rate peak-levels are practically unaffected by rise in elasticity. Alternatively, for the more polymeric-based fluid, such peak-levels are reduced with increasing elasticity. Successful attempts have been made to match rheological response and complex flow fields between strain hardening polymeric-based Oldroyd-B and constant shear viscosity FENE-CR models, so that the two fluids display the closest cross-slot flow field features. Here, similar stress field contours are observed for both models over a range of elasticity levels, with comparable pressure-drops. Similarly, strain hardening and strain softening e-PTT models are rheologically matched to SXPP models, which also provide insight into the distribution of molecular backbone-stretch. From the combination of viscometric data and numerical solutions for cross-slot flow, local peaks may be derived in strain-rate and maximum levels of normal stress may be accurately predicted with these models. This demonstrates a significant shift towards qualitative agreement with corresponding experimental findings.

1. Introduction

The shear and elongational deformation of viscoelastic fluids in complex flow configurations may have a significant impact on industrial material processing. In this respect, there is a real need to accurately predict such rheological response, both to optimise process design and to reduce production costs. Notwithstanding the importance of extensional flow properties in viscoelastic flows, yet all too often they have proved to be overlooked in practice. A number of measurement techniques have been introduced to determine these rheometrical properties, where each technique is known to have its advantages and disadvantages; see the detailed discussion in Macosko [1] and Morrison [2]. For example, this would include filament stretching, as in the apparatus devised by Sridhar et al. [3] for uniaxial extension, the apparatus of Meissner [4–6] for biaxial and planar extension, lubricated squeezing [7] for biaxial extension, use of contraction flow [8,9], the stagnation point using a four roll mill [9], and the cross-slot apparatus [10–12]. In spite of this position, still there exist relatively few reliable data-sets for such extensional flow configurations, due to the difficulty in generating homogeneous extensional flow. Moreover, breakdown may occur before reaching steady state, which may require long time-scales or large deformation conditions.

With cross-slot devices, a number of experimental investigations and numerical simulations have been performed to study the extensional rheology of polymer melts/solutions. For example, Schoonen [13] and Schoonen et al. [10] studied flow of 2.5% Pib/C14 polymer solution (2.5% (w/w) polyisobutylene dissolved in tetradecane) and LDPE in such cross-slot geometries. Their investigations closely matched experimental data with numerical predictions based on a DEVSS/DG algorithm. These authors used Geisekus and PTT viscoelastic constitutive models (CEs) as a basis to compare against a newly developed hybrid variant, the Feta-PTT model. This variant was derived by combining the PTT model with a viscosity function based on the modified Ellis model, proving useful in approximation of the Cox-Merz rule. Following this line of approach, Bogaerds et al. [14] performed cross-slot flow computations in three dimensions. Alternatively, Remmelgas et al. [15] employed a modified version of the finite element (*fe*) method developed by Singh and Leal [16] to simulate sharp-corner cross-slot flow with FENE models. This work involved various versions of the FENE model, with alternative conformation-dependent

* Corresponding author. Tel.: +44 1792 295656; fax: +44 1792 295708.
E-mail address: M.F.Webster@swansea.ac.uk (M.F. Webster).

0377-0257/$ – see front matter © 2009 Elsevier B.V. All rights reserved.
doi:10.1016/j.jnnfm.2009.05.001

ntributions to the friction coefficient term. The numerical results Remmelgas et al. for dumbbell-based constitutive equations ENE-CR and FENE-CD) were compared against experimental sults for ultradilute and finite concentration polymer solutions, monstrating reduction in the streamwise velocity for both mod-, relative to the Newtonian velocity field downstream of the gnation point (where the dumbbells are highly extended). How-er, the FENE-CR model was found to exhibit a birefringent strand th shorter length in the streamwise direction than that observed perimentally. Closer agreement was observed with the FENE- model, which gave a substantially more extended birefringent and downstream than that for the FENE-CR model with much wer relaxation from the extended state. As a follow up, Ver-eten [17] and Verbeeten et al. [11] extended the studies of hoonen [13] and Schoonen et al. [10] through the introduction the SXPP (Single-equation eXtension pom-pom) model. Encour-ingly, their numerical predictions with the SXPP model were und to lie in closer agreement with experimental findings, than s the case with Giesekus and PTT models. Experimental stud- were also reported by Coventry and Mackley [12], analysing a mber of optical birefringence patterns for cross-slot flows with range of polymer melts using the Multi-Pass Rheometer [18]. e stress birefringence patterns gathered were compared against merical solutions derived from PolyFlow (with integral CE, com-ercial package) and FlowSolve (with differential CE, Leeds U.) ftware, utilising various constitutive models. This birefringence ta revealed a wealth of information on rheology and structure verning the polymer melts involved, for unbranched low molec-ar weight polymers through to different levels of branching at w and high extension-rates. It was conspicuous however, that the lue of the predicted stress along the symmetry line around the gnation point disagreed with that gathered from experimental servation, and notably so in the case of highly branched or high olecular weight polymers. Moreover, Oliveira and co-workers [19] nsidered finite-extensibility models (FENE-CR and FENE-P) in a o-dimensional planar cross-slot geometry with sharp, 'slightly' d 'markedly' rounded corners. Their purpose was to analyse finite lume solutions and the contributing influences to the level of tensibility, concentration, and sharpness of corners, on the bifur-ted flow pattern above the critical *We*. Findings revealed that the furcation was unaffected by the rounding of the corner, but rather ntrolled by the extensional properties of the constitutive model, th a reduction in the level of the critical *We* for bifurcation as tensibility increased. More recent research has focused on micro-bricated cross-slot devices, specifically in accurate and low cost ethods for studying DNA [20].

The particular attraction of the cross-slot flow is that it offers ng-time exposure of some fluid elements to significant levels of tension when compared to say the deformation generated in a ntraction flow configuration. The key feature of cross-slot and her stagnation point flows is that the extensional strain asymp-es to infinity along the exit symmetry axis and therefore the flow fers, the ability to create an unlimited extensional strain at finite ain-rates, see [21]. Along the symmetry line of the cross-slot vice, the inflow fluid is compressed as it travels towards the stag-tion point, whilst outflow from this zone undergoes extension. e flow along this line is pure inhomogeneous extensional flow anar form, shear-free), and hence has only a non-trivial strain extensional component. Elsewhere in the domain, there are xed regions of high deformation, with both shear and extension. pure-extensional flow, the relationship between extensional formation rate and stress is prescribed through the extensional scosity, the ratio of normal stress difference to extension-rate. is is a 'strong flow' scenario where deformation increases expo-ntially with time, so that steady elongational viscosity is an ealisation. The extensional viscosity depends on the nature of the extensional flow type; uniaxial, biaxial, or planar. For the selected case of a Newtonian fluid, the uniaxial extensional viscosity is three times that of its constant shear viscosity; four times in planar extensional flow. The ratio of extensional to shear viscosity is known as the *Trouton ratio*, first used by Trouton [22] in 1906 and termed the 'coefficient of viscous traction'. The shear viscosity $\eta_s(\dot{\gamma}) = \lim_{t\to\infty} T_{xy}(\dot{\gamma})/\dot{\gamma}$ and extensional viscosity $\eta_e(\dot{\varepsilon}) = \lim_{t\to\infty} N_1(\dot{\varepsilon})/\dot{\varepsilon}$ are defined where $N_1(\dot{\varepsilon}) = (T_{yy}(\dot{\varepsilon}) - T_{xx}(\dot{\varepsilon}))$ is the first normal stress difference, $\dot{\gamma}(t)|_{t\to\infty} = \dot{\gamma}$ and $\dot{\varepsilon}(t)|_{t\to\infty} = \dot{\varepsilon}$ are the limiting steady-state shear-rate and the extension-rate, respectively. Here, T_{xy}, T_{xx}, and T_{yy} are components of total stress, where the principal component of extensional flow in the cross-slot is taken in the *y*-direction. The stress response in pure shear flow, (T_{xy}), is determined from the constitutive equation with knowledge of the velocity gradient $\nabla\mathbf{u}$ and shear-rate defined as, $\nabla\mathbf{u} = \begin{bmatrix} 0 & 0 & 0 \\ \dot{\gamma} & 0 & 0 \\ 0 & 0 & 0 \end{bmatrix}$. In a cross-slot device, sections of the flow have a pure planar elongational component, governed by normal stress response through T_{xx} and T_{yy}. Here, stress components are determined by the extensional deformation, with kinematics of $\nabla\mathbf{u}$ and strain-rate, $\nabla\mathbf{u} = \begin{bmatrix} -\dot{\varepsilon} & 0 & 0 \\ 0 & \dot{\varepsilon} & 0 \\ 0 & 0 & 0 \end{bmatrix}$. Accordingly, Trouton ratio in *planar* extension is defined as $Tr(\dot{\varepsilon}) = \eta_e(\dot{\varepsilon})/\eta_s(\dot{\gamma} = 2\dot{\varepsilon})$.

Pure shear and pure extension are two ideal instances of viscometric flow. Regions of complex flow may exhibit a mixture of these base flows, and where the elongational stress can dominate its shear counterpart in regions of active extensional deformation. Thus, in the present configurations of interest and notably in the case of severe strain-hardening models, the extensional viscosity can be utilised to qualitatively approximate the largest level of elasticity attainable (We_{crit}), providing a maximum extension-rate can be predicted on the pure extension line of the cross-slot flow.

In reporting cross-slot flow experimentally and numerically, birefringence measurement is often employed to represent the stress field and to quantitatively and qualitatively determine the fluid rheology. This technique relies upon the stress-optical law, which states that there is a linear relationship between the stress tensor and the deviatoric components of the refractive index tensor **n**, expressed in planar flows as [23]:

$$\Delta n = C\sqrt{N_1^2 + 4T_{xy}^2} = C \times PSD. \quad (1)$$

Here Δn is the difference in the refractive index, the birefringence, *C*, is the stress-optical coefficient (*SOC*), and $PSD = \sqrt{N_1^2 + 4T_{xy}^2}$ is termed the principal stress difference. As such, the birefringence patterns generated from experiments present discrete levels (bands) of constant stress. On the symmetry line, where the flow is shear-free ($T_{xy} = 0$), the principal stress difference identifies the normal stress difference, on the device walls, *PSD* equates to twice the shear stress; elsewhere *PSD* relates to both shear and extensional response.

2. Numerical modelling

In this study of cross-slot flow, the base numerical algorithm of choice is that of the hybrid finite element/finite volume form *fe*/*fv*(sc) based on pressure-correction methodology (see original version, Wapperom and Webster [24]). This scheme has been extensively documented and tested for various confined viscoelastic flows (see prior published work [25–27]) and is well-suited to the present task in-hand. Comment is passed below on comparatives performed with alternative algorithmic variants. The flow problem demands that velocity inlet and outlet boundary conditions

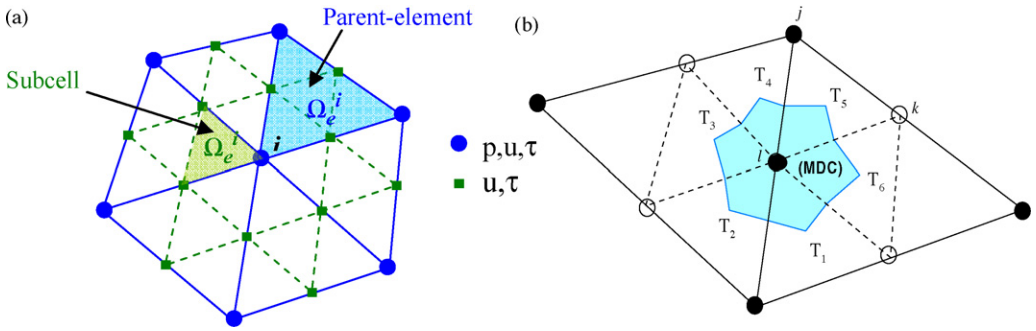

Fig. 1. (a) Parent *fe* and sub-cells tessellations and (b) *MDC* area for node *I*.

should be consistently posed according to the various constitutive equations, with appropriate provision for initial conditions to facilitate the time-stepping process. A quadratic polynomial shear-flow velocity profile is applied solely for Oldroyd-type or constant shear-viscosity constitutive models. The consequence of imposing improper boundary conditions, as in those with a mismatch of model, lies not only in the discrepancy between kinematics at the inlet/outlet regions of the domain, but is bound also within the pressure field response. To circumvent this complication for some of the nonlinear selected models of interest and for the sake of consistency, transient force-driven flow boundary conditions are also employed here, as detailed in [28]. Then, the pressure difference between inlet and outlet is fixed, as equivalent to that for an Oldroyd-B (constant viscosity), steady-state solution at any particular *We*-level and base flowrate setting. Then, the velocity is allowed to develop naturally across the flow domain in time to its selected steady state.

The relevant non-dimensional equation system for isothermal, viscoelastic, incompressible flow may be represented via conservation of mass and transport of momentum equations, supplemented by a constitutive equation for stress. For example, the system for an Oldroyd-B model may be expressed, viz.

$$Re\frac{\partial \boldsymbol{u}}{\partial t} = \nabla\cdot(2\mu_s\boldsymbol{D}+\tau) - Re\,\boldsymbol{u}\cdot\nabla\boldsymbol{u} - \nabla p, \tag{2}$$

$$\nabla\cdot\boldsymbol{u} = 0, \tag{3}$$

$$We\frac{\partial \tau}{\partial t} = 2\mu_p\boldsymbol{D} - \boldsymbol{\tau} - We(\boldsymbol{u}\cdot\nabla\boldsymbol{\tau} - \boldsymbol{\tau}\cdot\nabla\boldsymbol{u} - (\boldsymbol{\tau}\cdot\nabla\boldsymbol{u})^T), \tag{4}$$

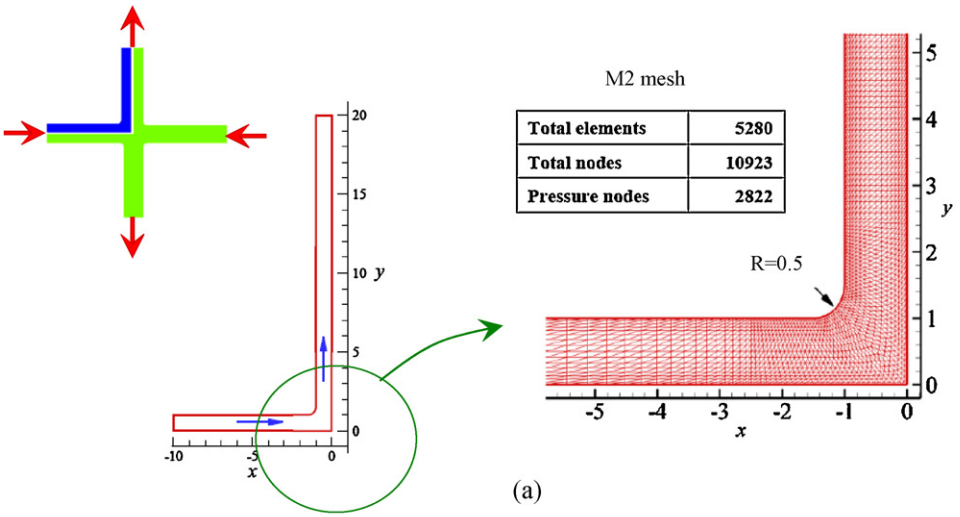

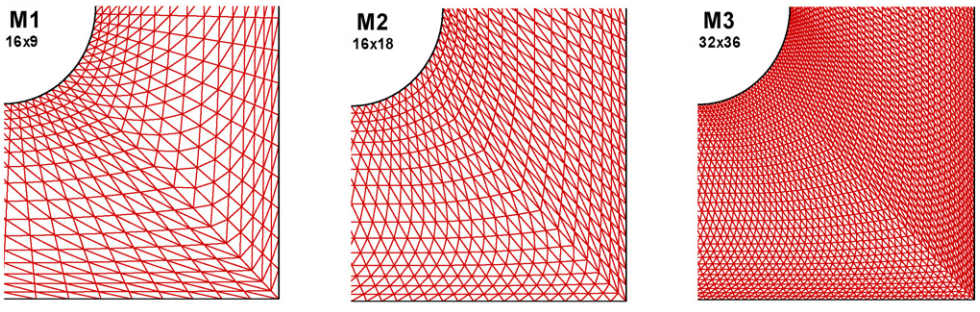

Fig. 2. Problem specification: (a) domain, flow direction, characteristic mesh and (b) mesh refinement (M1, M2, M3) detailed around the stagnation zone.

ble 1
terial functions for Oldroyd-B, linear-PTT and FENE-CR models.

del	Material function			Comment
	β	ε_{PTT}	L	
lroyd-B	0.9	–	–	Constant shear severe elongational
	1/9			
ear-PTT	1/9	10^{-4}	–	Shear thinning elongational level controllable
		10^{-3}		
		10^{-2}		
NE-CR	1/9	–	100	Constant shear elongational level controllable
			32	
			10	

here $\boldsymbol{u}$, p and τ represent the velocity, pressure, and extra-ess, respectively. Total stress may be segregated into viscous d elastic parts, $\boldsymbol{T} = 2\,\mu_s \boldsymbol{D} + \boldsymbol{\tau}$, and the rate-of-deformation tensor defined through the velocity gradients, $L^T = \nabla \boldsymbol{u}$, as $\boldsymbol{D} = (L + L^T)/2$. re, the zero shear viscosity is divided into polymeric (μ_p) and vis-us (μ_s) contributions, so that $\mu_0 = \mu_p + \mu_s$ with solvent-fraction $= \mu_s/\mu_0$. In addition, the dimensionless group parameters of ynolds number ($Re = \rho U \ell/\mu_0$) and Weissenberg number ($We = /\ell$) are introduced in Eqs. (2)–(4), dependent on material relax-on time, λ, density ρ, characteristic velocity scale U (average, low) and length scale ℓ (channel half-width).

Background detail on the time-stepping scheme and intermediate phases, inclusive of forward-time incremental pressure-correction (*PC*) may be found in our precursor studies [29,30]. For the sake of completeness, in this section we discuss briefly the key aspects involved. A time-stepping procedure of multiple fractional-staged equations is considered to solve the set of equations, based on the well-established Taylor-Galerkin Pressure Correction scheme. The *first phase* involves a Taylor-Galerkin scheme, expressed via a predictor–corrector doublet (Lax-Wendroff) for velocity and stress, which initially calculates a predicted half time-step velocity field $u^{n+1/2}$, prior to computing a non-divergence-free velocity field u^*. The *second phase* generates a Poisson-like equation for the time-step increment of pressure that ensures second-order accuracy in time ($\theta = 1/2$). A *third phase* is a correction step recapturing the solenoidal velocity field u^{n+1} at the end-of-time step loop. The *second and third phases* combined constitute the backbone of the pressure-correction scheme. By implementing a semi-implicit Crack–Nicolson treatment for diffusion terms (momentum equation), a semi-discrete incremental form of the scheme may be derived with improved stability and convergence properties. In addition, the incremental form of pressure-correction, with its three time-level reference, is known to be superior in uniform temporal error bounds over its non-incremental counterpart [31]. The finite element spatial discretisation is constructed around triangular elements based on quadratic interpolation for velocity and linear interpolation for pressure. Stress interpolation follows the particular scheme in question: either of finite element or cell-vertex finite volume, on parent or sub-cell reference, as required. For spatial discretisation, Carew et al. [32] employed a Galerkin *fe*-approximation

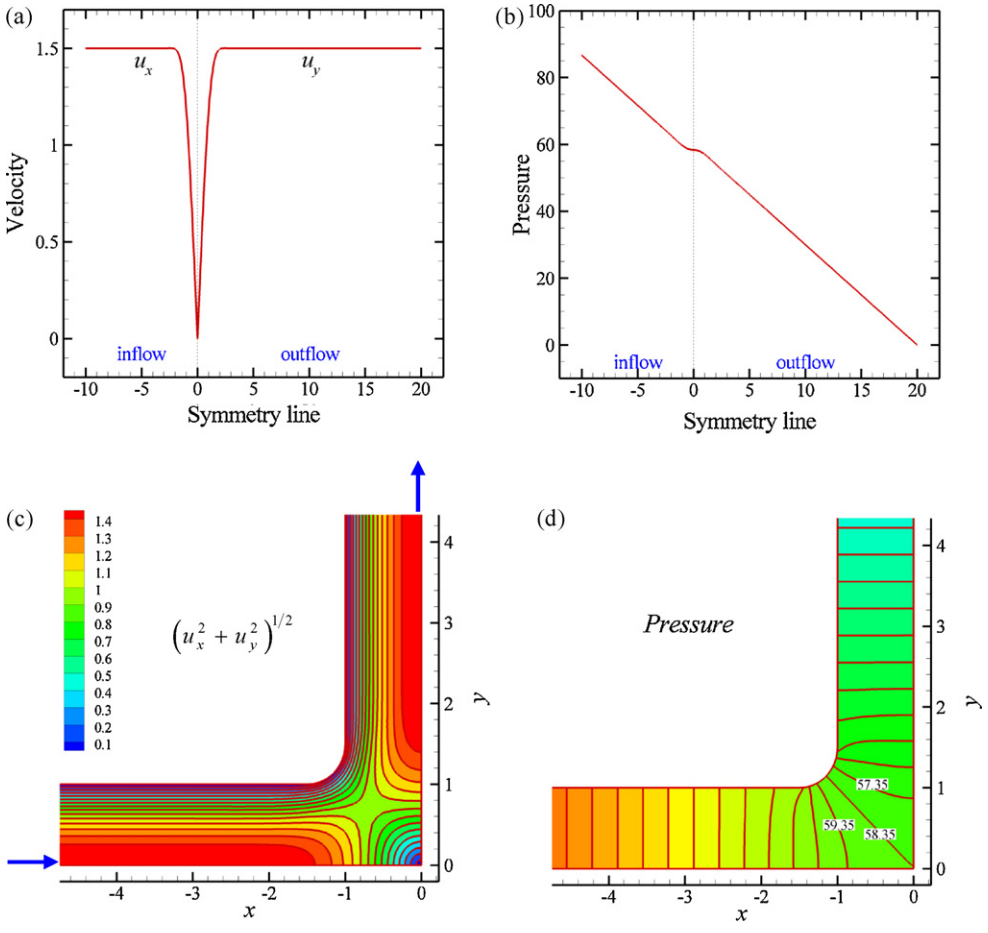

Fig. 3. Newtonian symmetry line velocity (a); pressure profiles (b); and respective contours (c and d).

Table 2
Material function for matching rheology between Exponential-PTT and SXPP models.

SXPP fluid model					Comment	Matching	Corresponding e-PTT fluid
No.	β	q	ε_{SXPP}	α			
1	1/9	8	0.999999	0.05	Strong-hardening	η_{pef}	$\varepsilon_{PTT} = 0.02$
2		5	0.5	0.15	Hardening	Tr	
3		2	0.333333	0.15	Delayed-softening	η_{pef}	$\varepsilon_{PTT} = 0.25$
4		2	0.075	0.15	Softening	Tr	

for velocity and pressure, with SUPG-quadratic weighting on stress. Alternatively, Wapperom and Webster [24] adopted a hybrid fe/fv scheme, as used here also, based on a Galerkin fe-approximation for mass-momentum balance and a cell-vertex fv-form for stress computation. The fe-grid may be utilised as a platform for the sub-cell fv-grid, which is composed of four sub-triangles, formed by connecting the mid-side nodes of the parent element. Stress variables are located at the vertices of the fv-cells and may be used directly as fe-nodal values without interpolation. Recently, and motivated by our earlier work on the hybrid fe/fv scheme, we have developed a further alternative for stress interpolation based on a pure fe-method at the sub-cell level [27,33,34] (akin to linear fe interpolation on the sub-cell). Such a novel fe(sc)-scheme may be implemented for cross-validation purposes against both the pure finite element discretisation at the parent-element level, fe, and the hybrid sub-cell scheme, fe/fv(sc) (see Fig. 1). Thus, investigating stability and demonstrating how stress and other solution features develop upon approaching critical states of elasticity, beyond which numerical divergence or temporal oscillations are encountered. Note that all three stress interpolation alternatives enjoy improved quality of velocity gradients, obtained via localised recovery procedures and applied over parent fe-elements (see Matallah et al. [35], Belblidia et al. [33]).

The geometric domain and characteristic meshing employed are depicted in Fig. 2, where due to symmetry assumptions, only one quarter of the flow domain is considered. The entry channel length is 10 U, whilst the exit channel length is 20 U, ensuring fully developed flow at the exit. No-slip boundary conditions are imposed on the wall. Inlet–outlet velocity boundary conditions are prescribed according to the fluid constitutive model. With constant shear constitutive models, as with Oldroyd-B and Finitely Extensible Non-linear Elastic-Chilcott Rallison (FENE-CR) models, the inlet–outlet flow in the device is prescribed with flowrate-driven boundary conditions (Waters and King type [36]). The force-driven protocol is employed for PTT and SXPP models, to avoid the distortion of pressure and stress fields from inconsistent inlet–outlet velocity boundary conditions. For inlet stress boundary conditions, each of the stress components is determined by solving the reduced pure-shear one-dimensional (ordinary) differential constitutive equation [28]. A preliminary mesh refinement analysis for the Oldroyd-B model has been conducted at $We = 0.1$ and $\beta = 1/9$, as performed elsewhere [27,37], where three levels of spatial discretisation have been considered to select the principal mesh (M2) employed in this work. The level of refinement is shown in Fig. 2 over the zoomed stagnation point section, where the refinement strategy ensures $O(1\%)$ change in stress solution between final successive meshes. For comparison purposes, mesh M2 employed in this study presents similar level of refinement across element topology to that utilised by Oliveira and co-workers [19] in the stagnation point region (block II). In this work, Newtonian and viscoelastic fluid models are considered, with material functions provided in Tables 1 and 2, and where Newtonian solutions are taken as a based reference for the viscoelastic calculations. Flows with the Oldroyd-B model are computed at two levels of solvent-viscosity fraction, $\beta = 1/9$ and 0.9, more and less polymeric constitution, respectively. Under homogeneous planar elongational flow, the Oldroyd-B model has a singularity at $\dot{\varepsilon}_{\text{sing}} = 1/(2\,We)$. In complex deformation configurations, this singularity renders the problem numerically challenging to solve when the extension-rate approaches the $\dot{\varepsilon}_{\text{sing}}$ level for the corresponding limiting We-value. Hence, this forms one of the key points of interest to study throughout this paper.

3. Numerical results and discussion

The numerical results are presented in three sections, subdivided across the constitutive models considered. Newtonian model findings are provided first for creeping and inertial flows (in Section 3.1). This is then followed by viscoelastic considerations through analyses for Oldroyd-B (Section 3.2), linear Phan-Thien–Tanner (L-PTT) and FENE-CR (Section 3.3), and exponential PTT (e-PTT) and pom-pom (SXPP, Section 3.4) models. Comparisons are performed throughout in terms of principal stress difference (*PSD*) patterns, commencing with Oldroyd-B and FENE-CR solutions. Although these two models have a constant shear viscosity, the Oldroyd-B model encounters singularity in extensional viscosity at $We = 1/(2\dot{\varepsilon})$, whilst the singularity is capped under the FENE-CR form. Further comparisons are performed subsequently between the FENE-CR and the linear PTT models. Matching material parameters for both models are sought at equitable levels of extensional viscosity, see Table 1. Note that the FENE-CR model displays a constant shear viscosity, whilst linear-PTT exposes shear-thinning behaviour. Finally, *PSD* patterns are contrasted, when matching either extensional viscosity or Trouton ratio for SXPP and e-PTT models, to confirm the nature and dominance of response under the complex deformation of cross-slot flow. Functional forms for shear and extensional viscosity with the various material models are provided in Appendix A.

3.1. Newtonian solutions

Solution fields for Newtonian flow are provided as a cross-reference to analyse additional viscoelastic effects in these

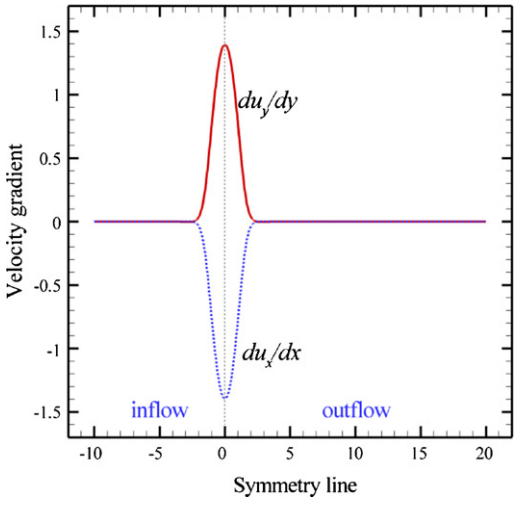

Fig. 4. Newtonian symmetry line strain-rate profiles.

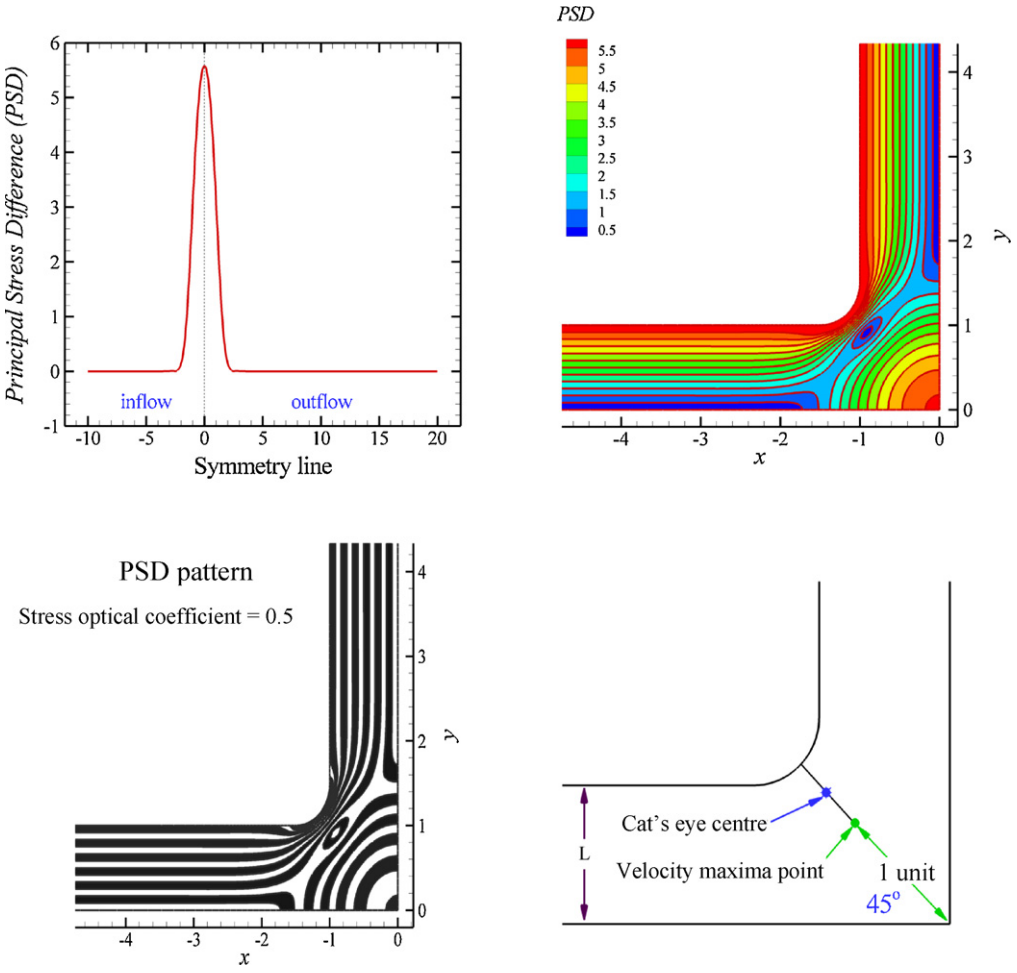

Fig. 5. Newtonian principal stress difference and the cat's eye feature.

oss-slot flows. Under Newtonian flow assumptions, the total ress is expressed as $\boldsymbol{T} = 2\,\mu_0 \boldsymbol{D}$ (no polymeric contribution), for hich it is instructive to systematically analyse velocity and pres- re solution across the whole domain and along the symmetry e from inlet to outlet. Initially, creeping Newtonian flow is con- lered. The dimensionless flow velocity on the symmetry line, picted in Fig. 3a, sustains a plateau level of 1.5 U *spanning* from the inlet and up to 2.5 U before the stagnation point. This is followed by a sharp u_x-velocity decline to rest at the device centre (0,0) (i.e. stagnation point). Beyond this position and symmetrically oriented, we observe an increase in u_y-velocity to reach the plateau level of 1.5 U at 2.5 U length from the centre. The sudden change in the velocity profile around the stagnation point is also felt locally in the pressure profile, as shown in Fig. 3b where the

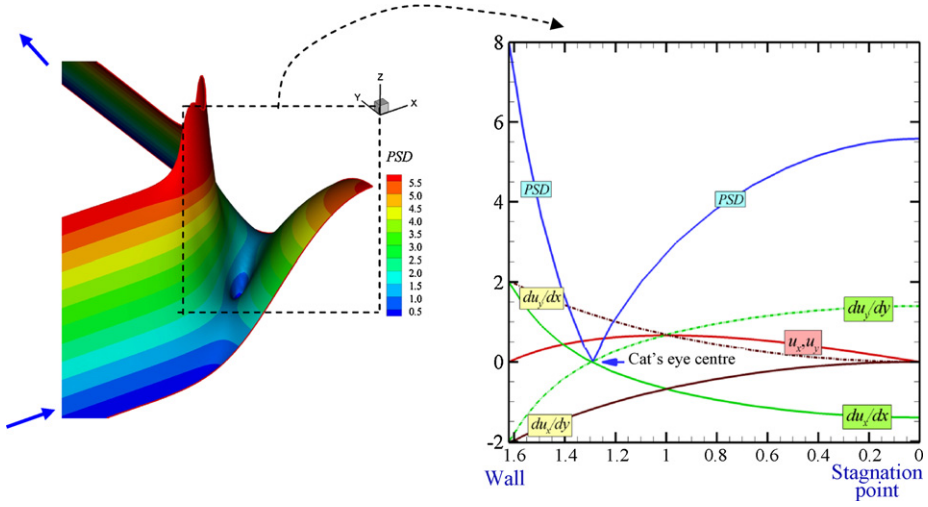

Fig. 6. Newtonian *PSD* in 3D plot (left) and velocity, velocity gradients and *PSD* across 45°-line from stagnation point to wall (right).

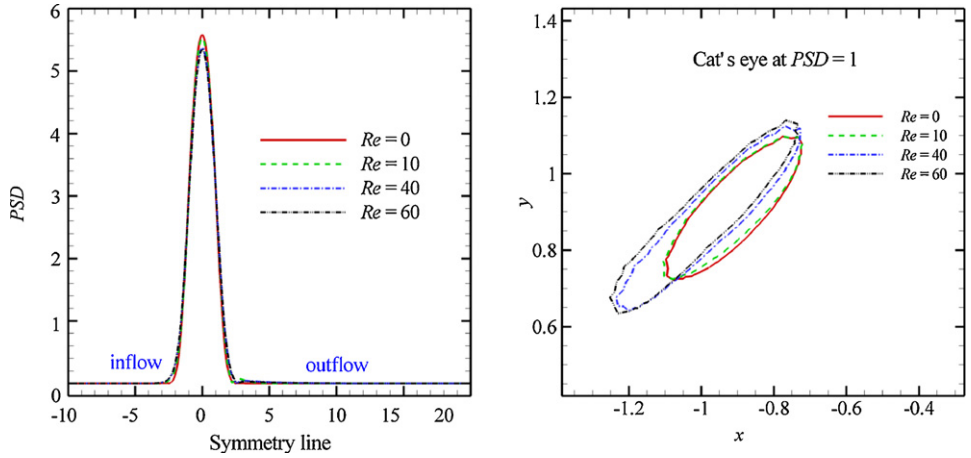

Fig. 7. Inertia effects on *PSD* profiles (left) and cat's eye (right) for Newtonian fluid.

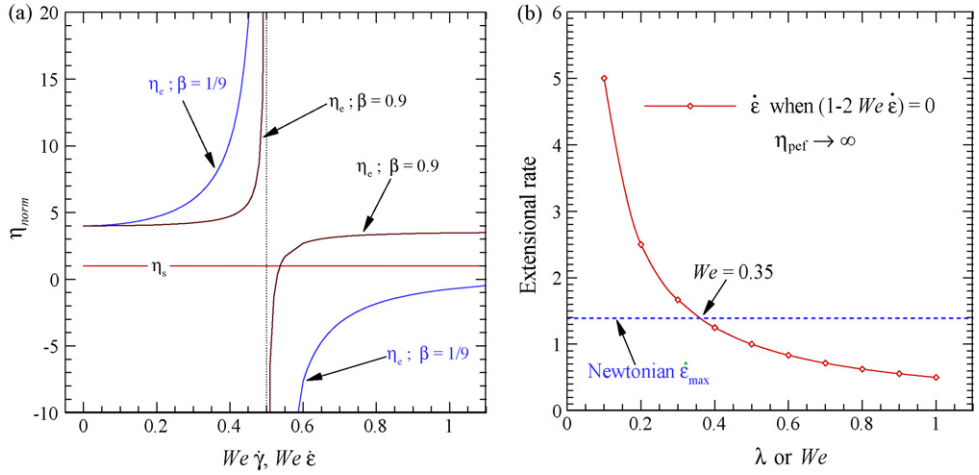

Fig. 8. Shear and elongational viscosities (a) of Oldroyd-B model for $\beta = 1/9$ and 0.9 and (b) predicted critical elasticity from maximum Newtonian strain-rate.

pressure linearly decreases from inlet to outlet. For completeness, the velocity magnitude $(u_x^2 + u_y^2)^{1/2}$ and pressure field contours are depicted in Fig. 3c and d, respectively. The location of maximum velocity (value of 0.935 U) is found at coordinate $(-\sqrt{2}/2, \sqrt{2}/2)$, a distance 1 U away from the centre on a 45°-line joining the device centre to the wall. Entry/exit flow pressure gradients are equal and constant, at a value of 3 U per unit length, departing only around the bend and in the localised stagnation point zone ($-2.5 \le x \le 0$ and $0 \le y < 2.5 < 0$).

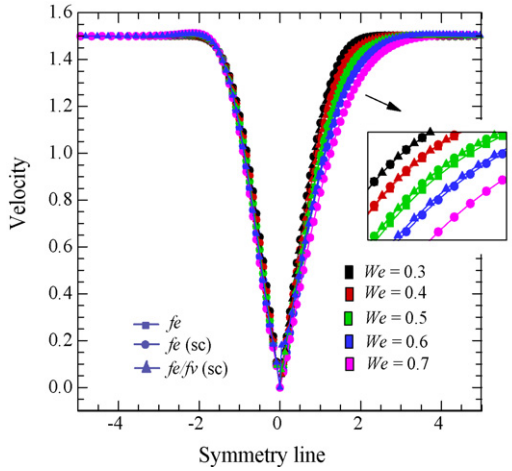

Fig. 9. Velocity profile on symmetry line for raising elasticity level and three numerical schemes, Oldroyd-B model.

The principal velocity gradients components, du_x/dx and du_y/dy, along the symmetry line from inflow to outflow are provided in Fig. 4. This plot confirms the accurate retention of conservation of mass (incompressibility enforced). The inflow velocity gradient component (du_x/dx) is negative, indicating the slowing down of the flow, with an opposite sign for the outflow velocity gradient du_y/dy. The maximum extension-rate magnitude of 1.4 U occurs at the stagnation point. Comparatively, this extension-rate figure is about triple that observed in the equivalent 4:1 planar contraction flow problem ($O(0.5)$ U [38]).

The *Principal stress difference* (*PSD*)-banding configuration is a conventional choice when attempting to make semi-quantitative comparison against experimental findings in the form of birefringence images. The *PSD* equates to the normal stress difference N_1 on the flow symmetry line (shear-free), and twice the shear stress ($2T_{xy}$) on the device walls. In a straight-channel pure shear flow, the shear stress and shear-rate, and therefore the *PSD*, are linearly dependent on the position normal to the direction of flow, that is, $\dot{\gamma}_{(y)} = du_x/dy$ and $T_{xy} = \eta_s \dot{\gamma}$. As such, the *PSD* structure is an equal-width black-and-white zebra-banding pattern parallel to the wall, indicating that stress levels are governed by the local shear-rate. For the cross-slot problem, we observe distortion from this shear

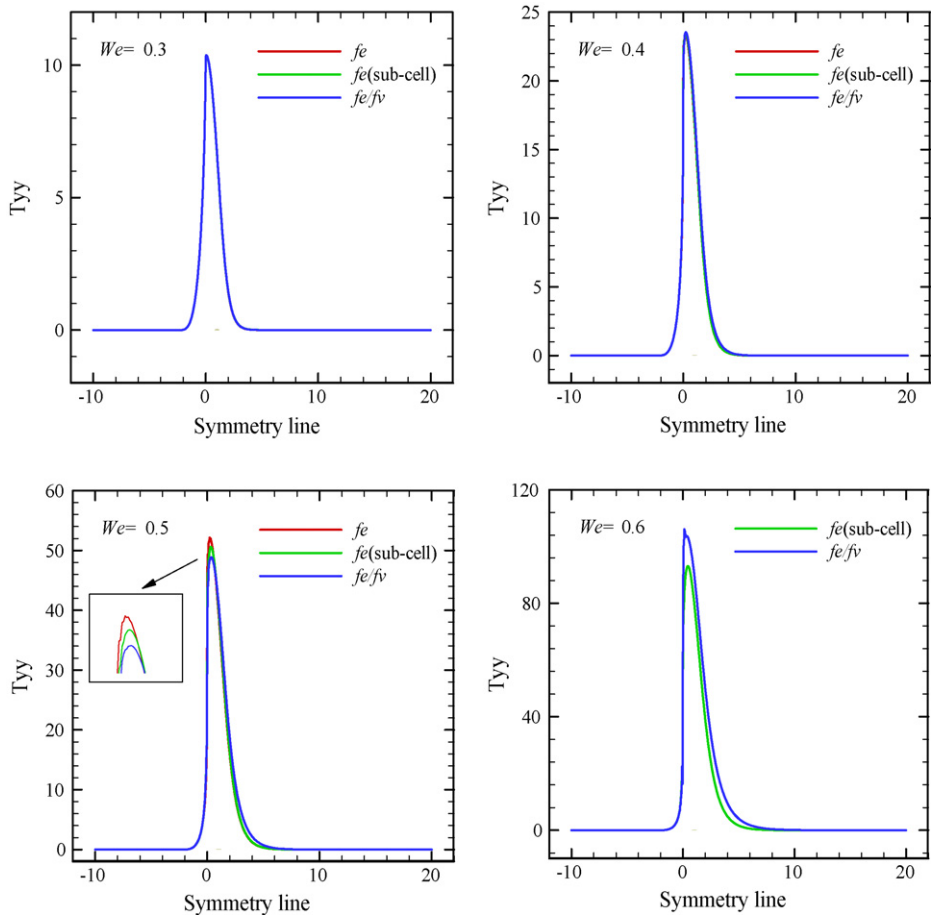

Fig. 10. τ_{yy} profile along the symmetry line for raising elasticity level and three numerical schemes, Oldroyd-B model.

w *PSD*-banding pattern at the device centre, highlighting a mix-re of pure shear flow and extensional flow; elsewhere along the low and outflow channel sections, shear behaviour is dominant. t, overall there is symmetry observed in the Newtonian banding ttern.

The complementary *PSD* field contour plot and *PSD* black-and-hite banding pattern are both depicted in Fig. 5. The stagnation int is clearly indicated at the centre of symmetry in the *PSD* ld, where the maximum *PSD*-value corresponds to four times e maximum extension-rate, that is a value of 5.6 U (as shown). is the presence and interaction of pure extensional and shear flow behaviour that causes the *PSD* cat's eye structure to emerge, as shown in Fig. 5 (zero *PSD*-level, shear stress counterbalances extensional stress). Plotted at the *PSD* level of unity, the cat's eye has an elliptical shape with its minor axis coinciding with the 45°-line joining the device centre to the opposing wall. For a Newtonian fluid, the zero *PSD*-level, where the cat's eye centre is located at (−0.927,0.927), lies just above the location where the maximum velocity occurs. For clarity of interpretation, Newtonian *PSD* in 3D plot perspective is provided in Fig. 6, alongside graphical representation for *PSD*, velocity, and velocity gradients across the 45°-line from the stagnation point to the wall (as shown in

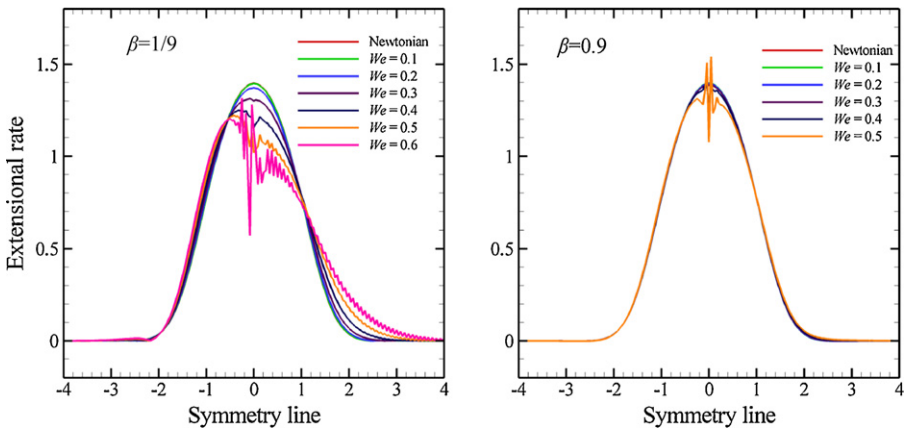

Fig. 11. Extension-rate along symmetry line, Oldroyd-B model, $\beta = 1/9$ (left) and $\beta = 0.9$ (right); *fe*|*fv* scheme.

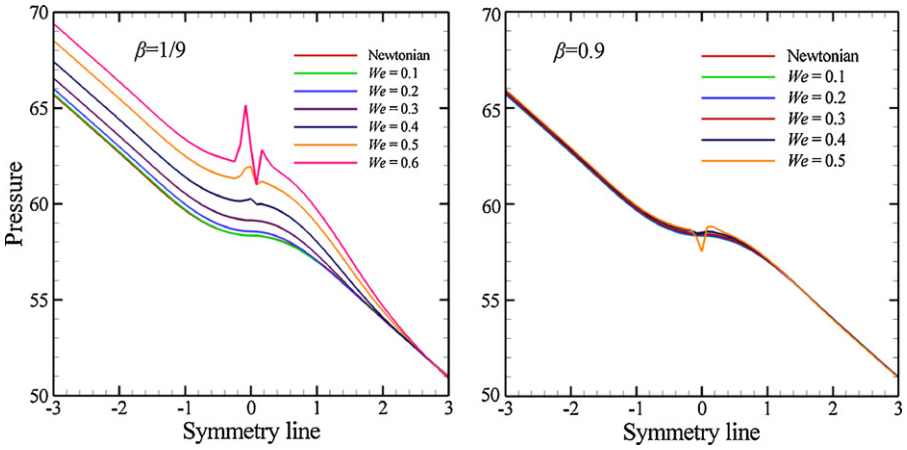

Fig. 12. Pressure profile along symmetry line, Oldroyd-B model, $\beta = 1/9$ (left) and $\beta = 0.9$ (right); *fe*/*fv* scheme.

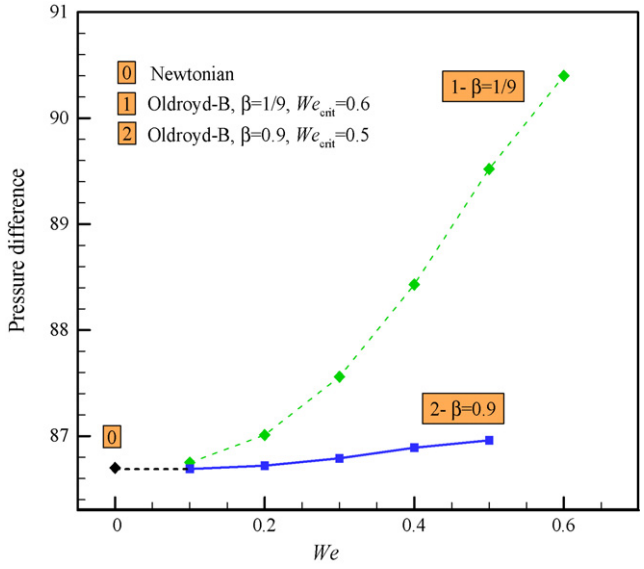

Fig. 13. Pressure profile with increasing *We*, Oldroyd-B model, $\beta = 1/9$ and 0.9; *fe*/*fv* scheme.

Fig. 5). At the centre of the cat's eye (zero-*PSD* level), extension-rate vanishes and the two shear-rate components, du_x/dy and du_y/dx, act in opposing directions, guaranteeing continuity satisfaction exactly. Use is made below of the departure from this symmetrical Newtonian feature as a benchmark to determine the fluid rheology for the various viscoelastic fluid models of current interest.

3.1.1. Inertial influence

Fig. 7 displays the *PSD* profiles along the symmetry line and the *PSD* cat's eye structure under Newtonian assumptions with four levels of Reynolds numbers (*Re*). The inertial level indicates the amplification of the convection term, $\mathbf{u}\cdot\nabla\mathbf{u}$, in the momentum equation. Clearly, on the symmetry line, the maximum value of *PSD* decreases with rising *Re* (about 5% decrease between $Re = 0$ and 60) without any other shift in the *PSD* plot. This stress peak reduction is also supported by the findings of Poole [39], where inertia has been noted to delay the onset of instabilities, whilst adding more nonlinearity to the problem. In the stagnation region, increasing levels of inertia cause the cat's eye feature to deform from the creeping flow elliptical-shape ($Re = 0$) to a more oblong shape. This deformation is more pronounced in the direction of the inflow, showing a slight shift towards the wall with increasing inertia.

3.2. Creeping viscoelastic flows: Oldroyd-B model

The Oldroyd-B fluid model, which is characterised as a constant shear-viscosity, strain-hardening nonlinear model, is often selected as a benchmark to develop numerical solutions in computational rheology. This popular nonlinear model manifests sufficient simplicity, yet also supports unbounded strain-hardening response. On symmetry lines, the flow is pure planar elongational, for which the Oldroyd-B shear and extensional viscosities, η_s and η_e respectively,

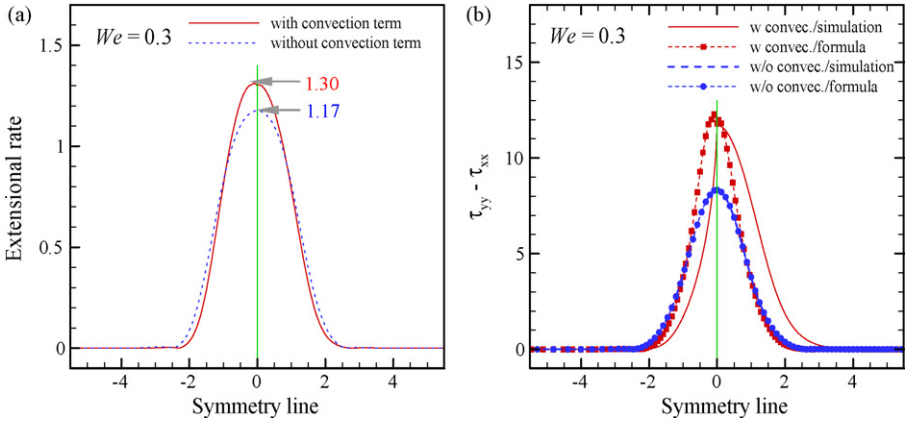

Fig. 14. Effect of convection term on extension-rate (a) and stress difference (b), Oldroyd-B modelat $We = 0.3$; $\beta = 1/9$; *fe*/*fv* scheme.

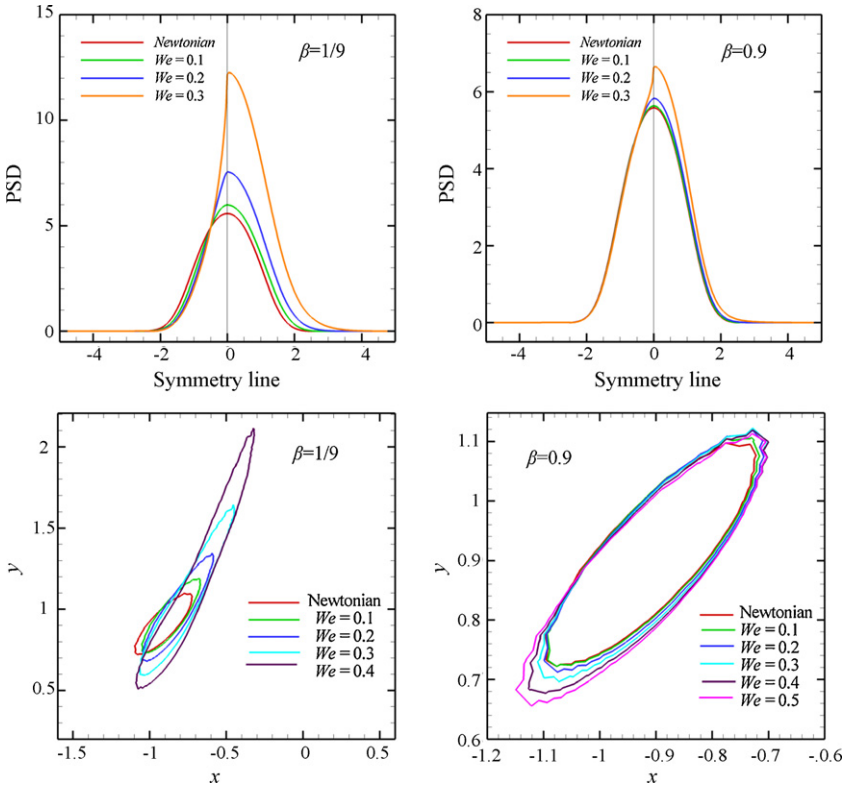

Fig. 15. *PSD* profile along symmetry line (top) and its cat's eye (bottom at *PSD* = 1 U), Oldroyd-B model, $\beta = 1/9$ (left) and $\beta = 0.9$ (right); *fe*/*fv* scheme.

e given analytically as

$$= \text{constant} = \mu_s + \mu_p, \tag{5}$$

d

$$= 4\mu_s + \frac{2\mu_p}{1 - 2\,We\dot{\varepsilon}} + \frac{2\mu_p}{1 + 2\,We\dot{\varepsilon}}. \tag{6}$$

From the expression of planar extensional viscosity as in Eq.), a singularity is observed at $We\,\dot{\varepsilon} = 0.5$, a contribution that ses due to the principal stress component (τ_{yy}) of the flow. e corresponding curves for shear and extensional viscosities are picted in Fig. 8a for two different solvent-fraction fluids: $\beta = 0.9$ d 1/9. With a more solvent-dominated fluid (approaching New- ian with $\beta \to 1$), the rise in extensional viscosity is delayed in $e\,\dot{\varepsilon}$ and is steeper than that for a more polymeric-based fluid.

Fig. 8b provides the plot of maximum extension-rate in contrast the critical elasticity level expressed by the singularity in the pla- r extensional viscosity ($1 - 2We\,\dot{\varepsilon} = 0$ in Eq. (6) and η_{pef} in Fig. 8). om the foregoing, the maximum extension-rate for a Newtonian id and this problem is determined as 1.4 U. Here, under Oldroyd-B id considerations, the critical elasticity level (We_{crit}) can be pre- cted, as illustrated in Fig. 8b, to occur at about 0.35 U. Essentially, is prediction assumes observations are taken in a Lagarangian me-of-reference (without stress convection) and where the max- um extension-rate is approximated to that experienced in the uivalent Newtonian flow field.

2.1. Critical elasticity states

With a view to investigating limiting elasticity solution lev- , consideration is given initially to the Oldroyd-B model with e solvent fraction $\beta = 1/9$ and flowrate-driven boundary condi- ns (Waters and King [30]). Here, solutions generated under the se scheme of choice in the hybrid *fe*/*fv* form, are compared and ntrasted against the two other variants of interest—the pure *fe* tions, in quadratic-*fe* and *fe* (sc). This provides both underpinning to the solution techniques employed and some insight as to solution trends concerning the singularity in the flow, its sharpness of capture and local restriction of subsequent numerical dispersion. Here, all simulations commence at the first Weissenberg solution level of $We = 0.1$ from quiescent initial conditions. Then, the Weissenberg number is incremented in steps of 0.1, and a continuation procedure enforced through initial conditions adopted from the immediate previous step. Successive steady-state calculations are performed by increasing *We* until the numerical scheme employed failed to converge, thus reaching the final critical solution state at We_{crit}.

Velocity profiles plotted on the symmetry line are provided comparatively in Fig. 9 for the zone surrounding the stagnation point, at increasing elasticity levels and with the three scheme variants cited. Up to an elasticity level of $We = 0.3$, these solution profiles prove independent of the scheme employed. Beyond this threshold $We \geq 0.4$, local discrepancies begin to appear in the velocity profile, on the outflow side just after the stagnation point (see zoomed insert), where there is a consistent downstream shift apparent through rising elasticity level. This solution feature is generated by the transition across the stagnation point and the particular variant of stress interpolation technique employed (see below). The position is confirmed through the inflow profiles, that are independent of both elasticity level and scheme implemented. Overall, critical solution states are established at $We_{\text{crit}} = 0.7$ with the *fe*(sc) scheme, $We_{\text{crit}} = 0.6$ with the *fe*/*fv* scheme, and $We_{\text{crit}} = 0.5$ for quadratic *fe*. This outcome may be understood when tracking the maximum value of τ_{yy} extracted per scheme, which provides an indication of the approaching critical state of elasticity with rising *We*. That is, as determined through the extensional viscosity (Eq. (6)), where the dominant contribution from the τ_{yy} extensional stress component is expressed as

$$\tau_{yy} = \frac{2\mu_p\dot{\varepsilon}}{1 - 2\,We\dot{\varepsilon}} \tag{7}$$

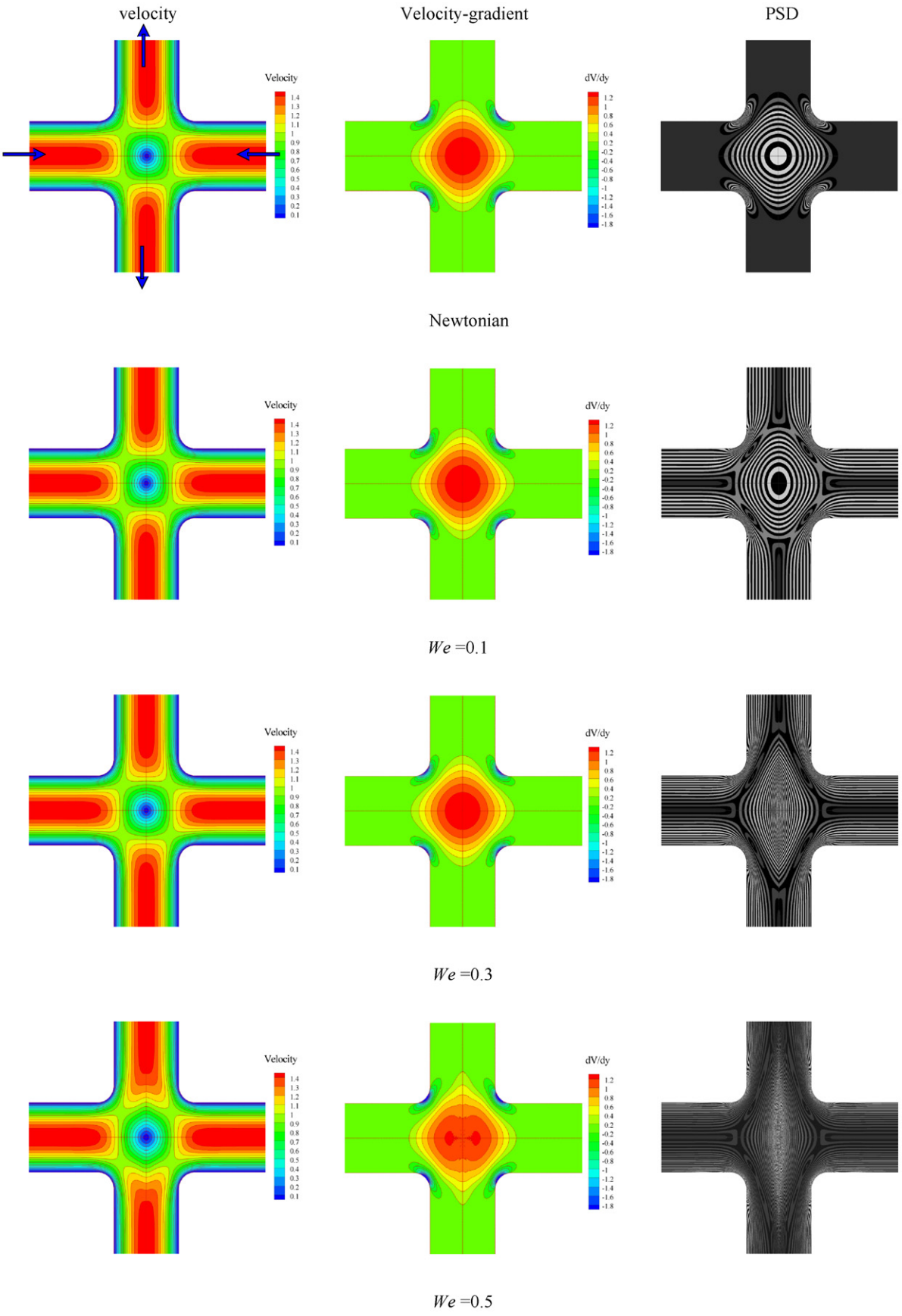

Fig. 16. Field contours on full domain: (left) velocity, (middle) velocity-gradient dV/dy, (right) principal stress difference birefringence ($SOC = 0.3$), with increasing We, Oldroyd-B model, $\beta = 1/9$; fe/fv scheme.

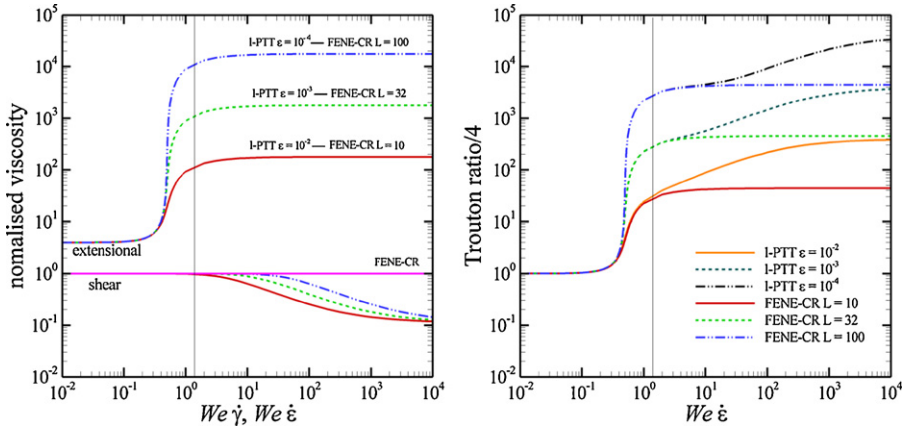

Fig. 17. Shear and planar extensional viscosities (left) and Trouton ratio (right), linear-PTT and FENE-CR models.

Hence, trends in the critical state of elasticity for each discrete proximation can be appreciated when analysing τ_{yy}-profiles ong the symmetry line, shown in Fig. 10. For $We \leq 0.4$, the τ_{yy} ess profiles and their maxima at the stagnation point are indis-guishable, and hence are independent of the scheme employed. fferences in maximum τ_{yy} are realised from $We = 0.5$ onwards (see om), being larger for *fe*-solutions in contrast to those for *fe*/*fv*(sc) d *fe*(sc) schemes; being the lowest for the *fe*(sc) scheme (see case $We = 0.6$). One notes the strictly local capture of the singularity all instances, which extends into the nonlinear regime for the droyd-B model, as in $We > 0.3$. In particular, the computed We_{crit} subject to the precise numerical treatment for stress introduced thin each scheme, which naturally throws up discrete differences the stagnation point zone (flow singularity). The superior sta-ity properties of the sub-cell schemes are borne out here, as served earlier for contraction flow problems [27]. There are only nor differences noted between the pure *fe*(sc) scheme and the brid *fe*/*fv* version, and hence, the more well-categorised hybrid rm is retained subsequently for further detailed consideration low. The analysis is taken forward by investigating the influence solvent-polymeric weighting constituting the Oldroyd-B param-erisation, covering high and low polymeric (low and high solvent) ctions. Based on the two levels of β-factor with the Oldroyd-B odel.

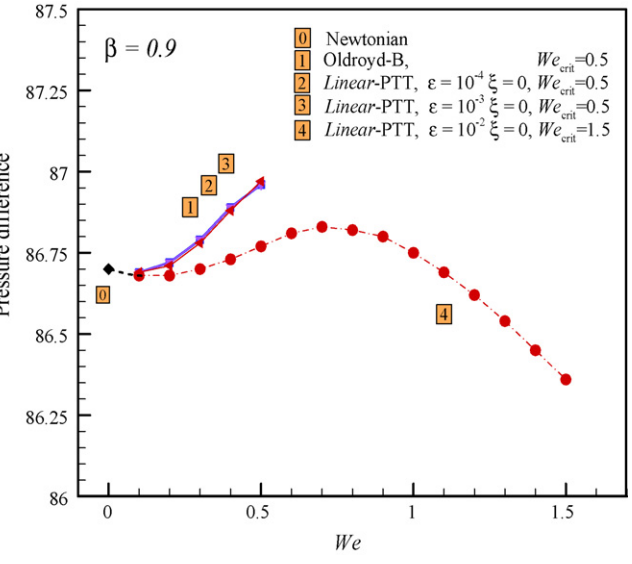

Fig. 18. Pressure drop for various constitutive models, $\beta = 0.9$.

Fig. 11 shows the profiles of extension-rate along the symmetry line using the *fe*/*fv*-scheme. For the more solvent-dominated fluid ($\beta = 0.9$), the deformation rate peak-level is practically unaffected by rise in elasticity. Alternatively, for the more polymeric-based fluid (smaller β value), the peak-level is reduced with increasing elasticity, accompanied by a rising trend in the downstream tail of the profile. Here, this stimulates the larger extensional viscosity values at a specific level of extension-rate for the more polymeric-based fluid (see Fig. 8a), and indicates that deformation variation arises mainly from the polymeric contribution of the fluid. As We_{crit} is approached, oscillations occur in extension-rate at the peak around the stagnation point, being larger in amplitude and frequency for the more polymeric-based fluids, and being constrained for the more solvent-based materials. Note that for these complex flows, numerical computations are still possible beyond the critical elasticity predicted by the pure theory and the singularity in extensional viscosity (see Fig. 8b). Fig. 12 provides profiles of the pressure along the symmetry line for the Oldroyd-B fluid with rising elasticity level at β and $\beta = 0.9$. As with Newtonian solutions above, there is a fluctuation in the profile near the stagnation point. These localised oscillations become larger with increasing elasticity, particularly for β (as noted in extension-rate, see Fig. 11). For $\beta = 0.9$, these oscillations are only apparent at relatively elevated levels of *We*, when $We = 0.5$. Interestingly, on the symmetry line, the pressure drop (inflow-outflow) for the more viscous fluid ($\beta = 0.9$) is unaffected by elasticity increase, whilst for the more polymeric-based fluid ($\beta = 1/9$), there is a distinct decrease in pressure drop (increase in upstream pressure level) as elasticity rises. This position can be contrasted against findings for the extension-rate above. Pressure difference inlet/outlet with increasing elasticity is depicted in Fig. 13 for the two solvent β-fractions. In contrast to the contraction flow problem, here the pressure drop increases as elasticity rises and there is a clear indication that the drop is considerably larger for the polymeric-based fluid ($\beta = 1/9$) in contrast to the solvent-based alternative (by about 3% at $We = 0.5$). In contrast, for $\beta = 0.9$, there is a negligible increase at $We = 0.5$ of about 0.3% above the Newtonian pressure. Such pressure drop trends are in keeping for the extension-dominated cross-slot flow above the contraction flow, noting also that the former is devoid of vortex response.

3.2.2. Constitutive model without stress convection

To facilitate comparison with theoretical solutions, the constitutive equation for the Oldroyd-B fluid at $\beta = 1/9$ may be solved, by omitting the convection term $\mathbf{u}\cdot\nabla\boldsymbol{\tau}$ from the stress equation. Under this option, the critical elasticity level is found to reach $We_{crit} = 0.3$, a level around that predicted by the critical extension-rate plots of Fig. 8. One notes that this critical level has risen to $We_{crit} = 0.6$

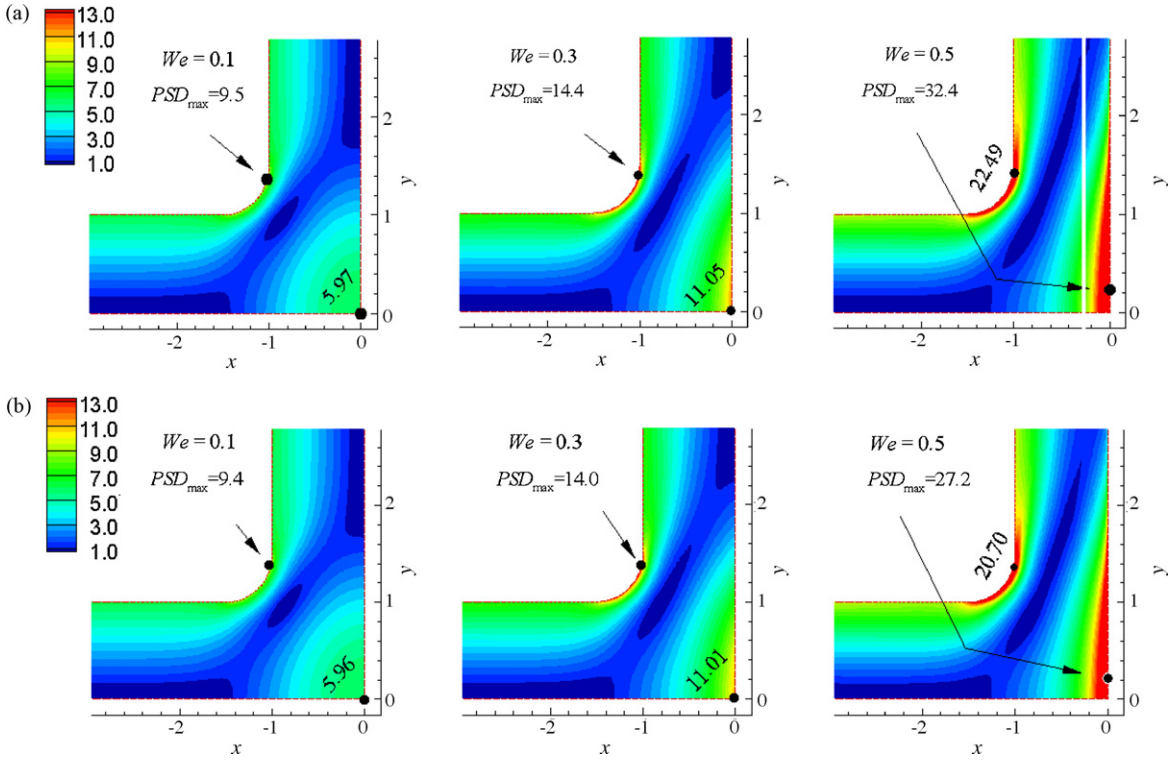

Fig. 19. *PSD* patterns with increasing elasticity of (a) linear-PTT model with $\varepsilon = 10^{-2}$ and (b) FENE-CR with $L = 10$.

when the convection term is retained (complex nonlinear, Eulerian setting). Extension-rate profiles along the symmetry line for the constitutive equation both with and without the convection term at $We = 0.3$ are presented in Fig. 14a. Clearly, both profiles are symmetric and the fluid has a lower maximum extension-rate when stress convection is ignored (see Mackley and Coventry [12], Coventry [40]). Yet, this position will also affect the levels of stress supported accordingly.

With known extension-rate $\dot{\varepsilon}$, the polymeric stress difference $(\tau_{yy} - \tau_{xx})_{\eta_e}$ along the cross-slot symmetry line may be evaluated from the expression for extensional viscosity, viz.

$$(\tau_{yy} - \tau_{xx})_{\eta_e} = (\eta_e - 4\mu_s)\dot{\varepsilon}. \tag{8}$$

To analyse the effect of stress convection on the polymeric stress difference, a comparison through two different procedures is conducted, utilising computations based on constitutive equations both with and without the convection term. Alternatively, such stress differences can be evaluated from a prescribed extension-rate and extensional viscosity formula via Eq. (8). From Fig. 14b, both calculations (formula *vs.* simulation) provide matching stress difference in the absence of the convection term. This is to be anticipated, as the normal stress evaluated from extensional viscosity in pure extension (η_e) does not account for the inclusion of stress convection. Therefore, its profile is symmetric around the stagnation point, as is the case for the extension-rate profile (Fig. 14a). The presence of nonlinearity via the convection term in the simulations causes the normal stress difference to shift downstream to the right-hand side (asymmetric), in contrast to its counterpart evaluated from η_e based on the predicted extension-rate from the nonlinear regime simulation with the convection term (see Mackley and Coventry [12], Coventry [40]). These latter two alternatives that take account of convection, also reach slightly different maximum levels. Moreover, this demonstrates how the extensional response in pure elongation (neglecting convection) can be effectively deployed as a tool to qualitatively predict stress behaviour in such a cross-slot flow deformation field, deriving close proximity in stress difference maxima as required. What is vital is precise knowledge of the extension-rate in situ. These strain-rate values at $We = 0.3$ (Fig. 14a) can be utilised to improve the estimated Newtonian maximum strain-rate in the arguments surrounding Fig. 8 to re-evaluate critical elasticity levels for the Oldroyd-B fluid. From Fig. 14a, the maximum strain-rate without convection is 1.17 U, giving $We_{\text{crit}} = 0.42$, whilst that with convection is 1.30 providing $We_{\text{crit}} = 0.38$; the localised trend with rising *We* is one of the increasing We_{crit}.

3.2.3. Principal stress difference and cat's eye phenomenon

The *PSD* along the symmetry line and *PSD* cat's eye structure with rising elasticity level are considered in Fig. 15 for the Oldroyd-B fluid and two solvent fractions, under $\beta = 1/9$ and 0.9. For the more solvent-based fluid ($\beta = 0.9$), the *PSD* profiles and cat's eye feature closely approximate Newtonian findings of Fig. 7 ($Re = 0$). In contrast, for more polymeric-based fluids ($\beta = 1/9$), the *PSD* maximum level increases exponentially with rising elasticity. Due to the presence of the stress convection term in the simulation (as discussed above), *PSD* profiles shift downstream towards the outflow, being more pronounced at larger *We*, as greater elasticity amplifies the convection term contribution. The position is similar for the variation in the shape of the cat's eye (plotted at *PSD* level of 1.0) and with regard to increased elasticity; this becomes more prominent for the less viscous fluid ($\beta = 1/9$) in contrast to the less polymeric alternative ($\beta = 0.9$). The elongation of the cat's eye is more oriented towards the outflow for $\beta = 1/9$. If this trend were to continue with rising *We*, one may envisage a situation where the elongation/distortion of the cat's eye structure becomes such that the width of this region will trend to vanish. The structure and orientation of the cat's eye in itself provides a visual reflection of the fluid rheology through the stress response. In these situations of highly distorted cat's eye, one may anticipate that the corresponding experimental birefringence-banding pattern cannot be clearly distinguished, see Coventry and Mackley [12].

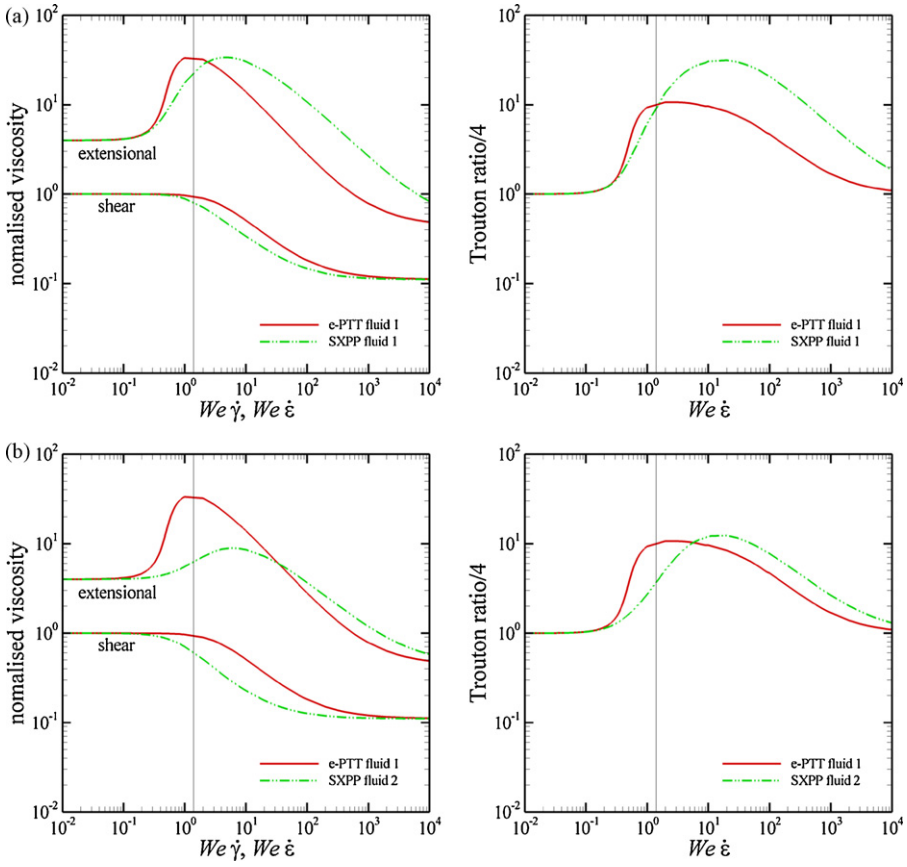

Fig. 20. Material functions for matching extensional rheology (left) or Trouton ratio (right) of e-PTT model with $\varepsilon_{PTT} = 0.02$ with (a) SXPP fluid 1 (b) and SXPP fluid 2.

The three fields of Fig. 16 complement the above information, splaying left to right, velocity field, velocity-gradient and *PSD* con-urs, with increasing elasticity (*We*) top to bottom from Newtonian *Ve* = 0) in increments of 0.1. The Newtonian square central veloc- pattern is accompanied with a dented-diamond shape (lozenge) locity-gradient and *PSD* pattern. Peaks are also located around e corners; symmetry is upheld in all three fields. Distortion is parent with increasing *We*, notably at *We* = 0.5: in the exit channel wnstream of the stagnation point in velocity and its gradients; o just upstream of the stagnation point in velocity-gradient; *PSD* tterns show the central stretched configuration along the exit ne and elongation of the cats' eye feature.

3. Comparison through L-PTT, FENE-CR and Oldroyd-B solutions

The rheological attraction of these models is that under the ear thinning Linear Phan-Thien–Tanner (L-PTT) model, the severe tensional viscosity at $We = 1/(2\,\dot{\varepsilon})$ occurring under the Oldroyd- model is removed. This finite extensional response is found o with the Finitely Extensible Nonlinear Elastic-Chilcott Rallison ENE-CR) model, governed by the single Hookean-spring length rameter *L*. The L-PTT model has two additional material param-ers $(\varepsilon,\xi)_{PTT}$, see Appendix A; the maximum extensional viscosity controlled by the parameter $\varepsilon \geq 0$, whilst the parameter $0 \leq \xi \leq 2$ odifies the shear viscosity and second normal stress difference efficient. As $\varepsilon \to 0$, the larger the maximum value of extensional scosity becomes. In the limit when $(\varepsilon,\xi) = (0,0)$, the Oldroyd-B odel is recovered with unbounded extensional response. Note, roughout this work, the material parameter ξ is set to zero when ing the PTT model, rendering a zero second normal stress differ-ce coefficient.

The viscometric plots for L-PTT and FENE-CR models are supplied in Fig. 17. This includes plots for shear and planar extensional viscosity, alongside corresponding Trouton ratios. Matching extensional viscosities can be derived for both L-PTT and FENE-CR models, dependent upon precise choice of material parameters (ε for L-PTT and *L* for FENE-CR, see Table 1). The shear and planar extensional viscosities of L-PTT and FENE-CR model are identical for low values of deformation rate, independent of material parameters. This is followed by a sharp rise in extensional viscosity to reach a plateau at high extension-rates, levels of which depend upon parameter selection. The strain hardening is more severe with smaller ε for L-PTT, or larger *L* for FENE-CR. The shear viscosity is, by construction, constant for FENE-CR, whilst it reflects shear-thinning behaviour for the L-PTT model. Consequently, the Trouton ratios (defined above) for the two models begin to depart above a certain threshold of extension-rate, as shear viscosity is non-constant for the L-PTT choice.

The critical elasticity level of L-PTT model is dependent on material parameter selection of β and ε. For small material parameter $\varepsilon \leq 10^{-3}$, the We_{crit} and pressure drop for L-PTT and Oldroyd-B fluid models are practically equivalent. The pressure drop, depicted in Fig. 18, is observed to rise with increasing elasticity for $\varepsilon \leq 10^{-3}$. In contrast, for $\varepsilon = 10^{-2}$, the pressure drop increases with *We* until *We* = 0.7, where it reaches a maximum (a level lower than that for $\varepsilon \leq 10^{-3}$ case), followed by a gradual decline thereafter. In contrast, under the contraction flow problem, the trend in pressure-drop was initially decreasing with rising elasticity, independent of PTT material parameters (see [38]).

Similar planar extensional response can be established for L-PTT ($\varepsilon = 10^{-2}$, $\xi = 0$) and FENE-CR ($L = 10$), as shown in Fig. 17. Utilising such settings, corresponding *PSD* patterns are provided in Fig. 19, where one may contrast the stress field position at rising elasticity

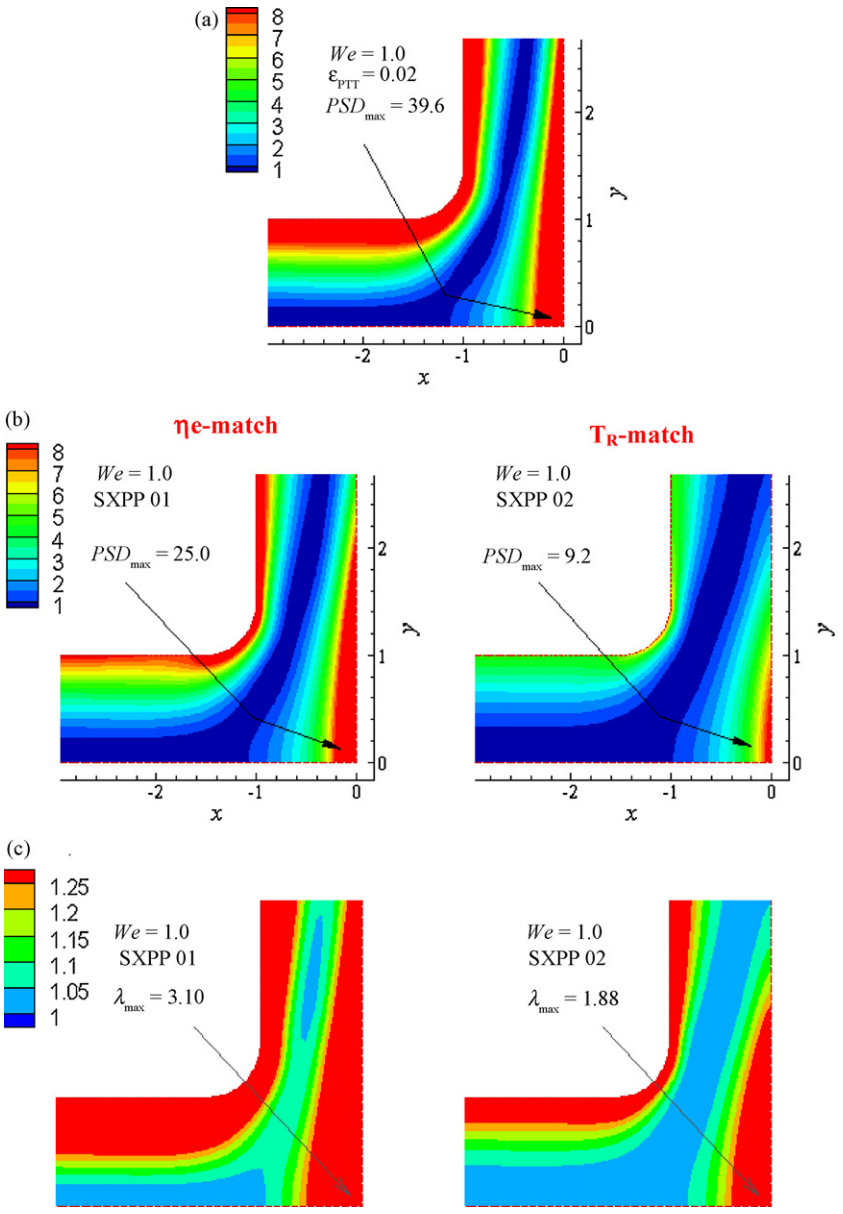

Fig. 21. The *PSD* patterns of (a) e-PTT with $\varepsilon_{PTT} = 0.02$ and its corresponding (b) SXPP model matching and (c) backbone-stretch fields.

(*We* = 0.1–0.5). Here, the *PSD* contours are plotted at 1 U increments between contours, with the *PSD* zero-level established on the symmetry line in the pure shear flow zone. The plotting scale is adopted from *We* = 0.1 solutions, to expose the growing magnitudes with rising *We*, accompanied by the relevant maxima achieved in each case. The peaks of *PSD* values in the problem can be isolated at the wall-bend (shear-dominated, indicates T_{xy}-levels) and on the symmetry line (extension-dominated, provides N_1-levels), downstream of the stagnation point. Over this range of *We*, the distribution and orientation of *PSD* contours are similar for both models, with minor differences becoming apparent at *We* = 0.5 in the shape of the cat's eye. Any differences noted are attributable to the shear-thinning properties of the L-PTT model, as can be observed particularly around the bend and at the high-shear region near the wall of the geometry. Larger levels of stress in *PSD*-maxima are noted for L-PTT (32.4 U) over those with FENE-CR (27.2 U), noting that force-driven protocols on PTT results maintain comparable pressure-drops across the flow and elevated shear-rates to compensate for decline in viscosity. There are little differences detected in the extension-dominated symmetry line zone, a position largely reflected throughout the domain demonstrating the greater influence of η_e in such a flow.

3.4. Matching rheology: Pom-Pom (SXPP) and e-PTT models

By way of background, we cite the related work reported in two earlier articles on contraction flows with various models, paying particular attention to vortex behaviour with rising elasticity level (*We*-rise). The prior study of Aboubacar et al. [38], contrasted field solutions for Oldroyd and PTT (exponential/linear) models in a range of contraction flow scenarios—planar/axisymmetric, abrupt and rounded-corner cases. Subsequently, Aguayo et al. [30] performed matching on extensional properties across two different types of constitutive models in planar rounded-corner 4:1 contraction flows, focussing on the comparison between network-based exponential Phan-Thien–Tanner (e-PTT) and kinetic-based SXPP models, seeking parity on vortex behaviour. This work picked out two choices of e-PTT model from those used by Aboubacar et al. [38], that is with $\varepsilon_{PTT} = 0.02$ to characterise severe strain hardening and $\varepsilon_{PTT} = 0.25$ for modest strain-hardening properties. For each

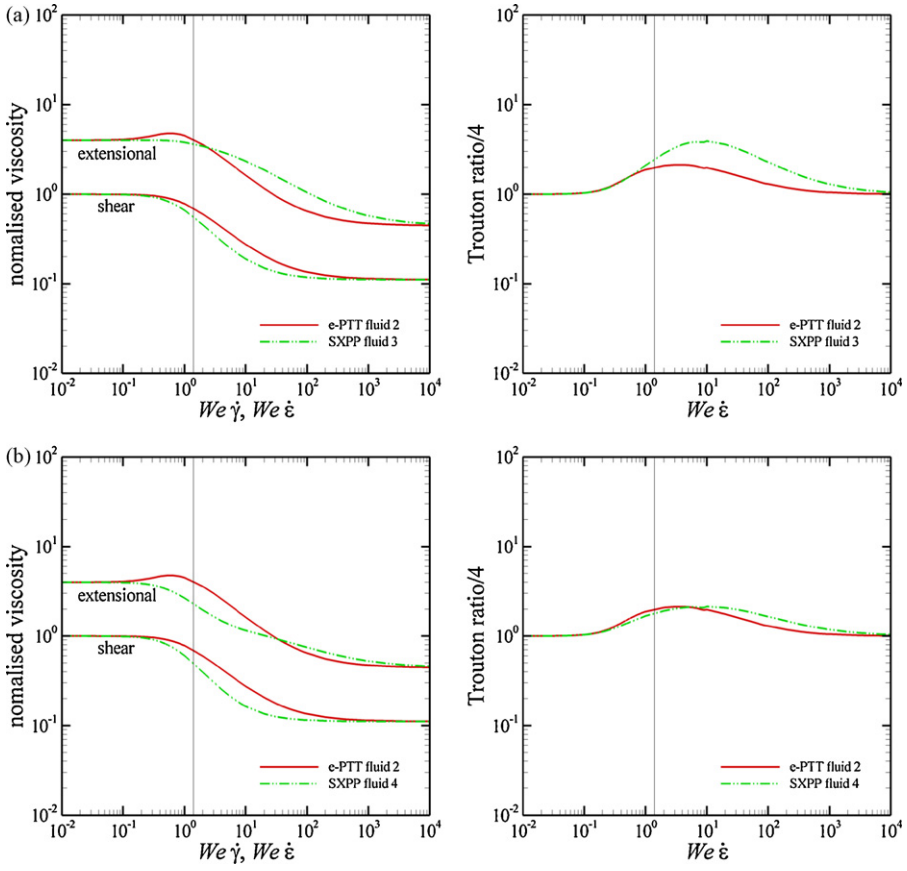

Fig. 22. Material functions for matching extensional rheology (left) or Trouton ratio (right) of e-PTT model with $\varepsilon_{PTT} = 0.25$ with (a) SXPP fluid 3 and (b) SXPP fluid 4.

PTT fluid a match was configured on peak extensional rheol-y response against its SXPP model counterpart. The match was ganised according to two alternative criteria: sought on *maximum* anar extensional viscosity (peak-η_e) or corresponding *maximum* outon ratio (peak-*Tr*)—generating four base fluid options. The out-me was reported in terms of vortex enhancement characteristics, mparing and contrasting measures of vortex cell-size and vor-x intensity across models and material parameters. In the *strong ain-hardening* regime, findings revealed that matching on the ak-η_e stimulated the largest vortex enhancement but also the west We_{crit}. Matching instead on peak-*Tr*, lessened vortex activity hilst doubling We_{crit}. Alternatively, under the *moderate strain-rdening* regime, vortices significantly diminished in contrast to der the *strong strain-hardening* regime, ultimately leading to rtex inhibition at larger deformation rates. Here, only slight dis-ction could be drawn between the extensional matching options, ting only slight vortex enhancement at early levels of elasticity th that on peak-η_e, whilst matching on peak-*Tr* lead to imme-ate and sustained vortex reduction. A similar line of analysis is nducted here for the two *strain-hardening* regimes and the four PP fluids of Table 2 (with model parameters and comment on cor-sponding rheology, see Appendix A for corresponding equations d parameters), but now in the current cross-slot flow configura-n and with *PSD* response the main feature in mind. Note, that th the SXPP constitutive model, the maximum peak in exten-nal viscosity is constrained by two parameters, the number of olecular side arms (q) and the ratio of the relaxation times (ε_{SXPP}). is ratio of relaxation times not only affects the maximum peak the extensional viscosity, but also its rate (angle) of rise, an usive feature to capture under SXPP modelling at the rapid rate pressed in Oldroyd-B/e-PTT strongly strain-hardening mode. Fur-ther detailed discussion on a suitable selection of parameters for SXPP-fluid 1 to SXPP-fluid 4 and their rheology is provided in [30]. One notes, for these SXPP-fluids, values of $\alpha \leq 0.15$ are used, following rheological arguments in [30] on improved matching for η_e and reduced N_2-influence. One has to be careful to avoid some mathematical and rheological deficiencies of the SXPP-model. In particular, the use of a non-zero α (Geisekus) parameter to realise the introduction of N_2, may cause some difficulties giving rise, for example, to bifurcations or multiple solutions [41]. Here, to avoid such issues, the number of arms (q) is restricted to a maximum of 8 when $\alpha = 0.05$ and no larger than 5 when $\alpha = 0.15$.

3.4.1 Matching η_e and Tr for strong strain-hardening e-PTT ($\varepsilon_{PTT} = 0.02$) and SXPP models

The shear and planar extensional viscosities, including the corresponding Trouton ratio, for e-PTT fluid (fluid 1, $\varepsilon_{PTT} = 0.02$) and their corresponding SXPP match on η_e (SXPP-fluid 1) and on *Tr* (SXPP-fluid 2) are illustrated in Fig. 20a and b, respectively. Salient features to draw out, when interpreting for a fluid of $We = 1$ as below, are the following. Against SXPP-fluid 1 data, matching η_e maxima of $O(30\,U)$ are observed, occurring a decade earlier with e-PTT fluid 1 over SXPP-fluid 1. This goes hand-in-hand with the earlier more rapid rise in η_e for e-PTT in the deformation range $0.3 < \dot{\varepsilon} < 2$ and reappears in *Tr*, where there is a clear switch-over in dominant response between the fluids beyond the $(\dot{\varepsilon} = 1.4)$-line, as indicated. In shear, e-PTT response is delayed in thinning by about one decade over that for the SXPP-fluid 1, justifying the enhancement observed in *Tr*. In contrast, considering the SXPP-fluid 2 data, scaled *Tr* maxima of $O(10\,U)$ are exposed, at deformation rates around $\dot{\varepsilon} = 1$ for e-PTT fluid 1 and $\dot{\varepsilon} = 10$ for SXPP-fluid 2. This provides η_e maxima that differ by a factor of three in magnitude, with η_e maxima of

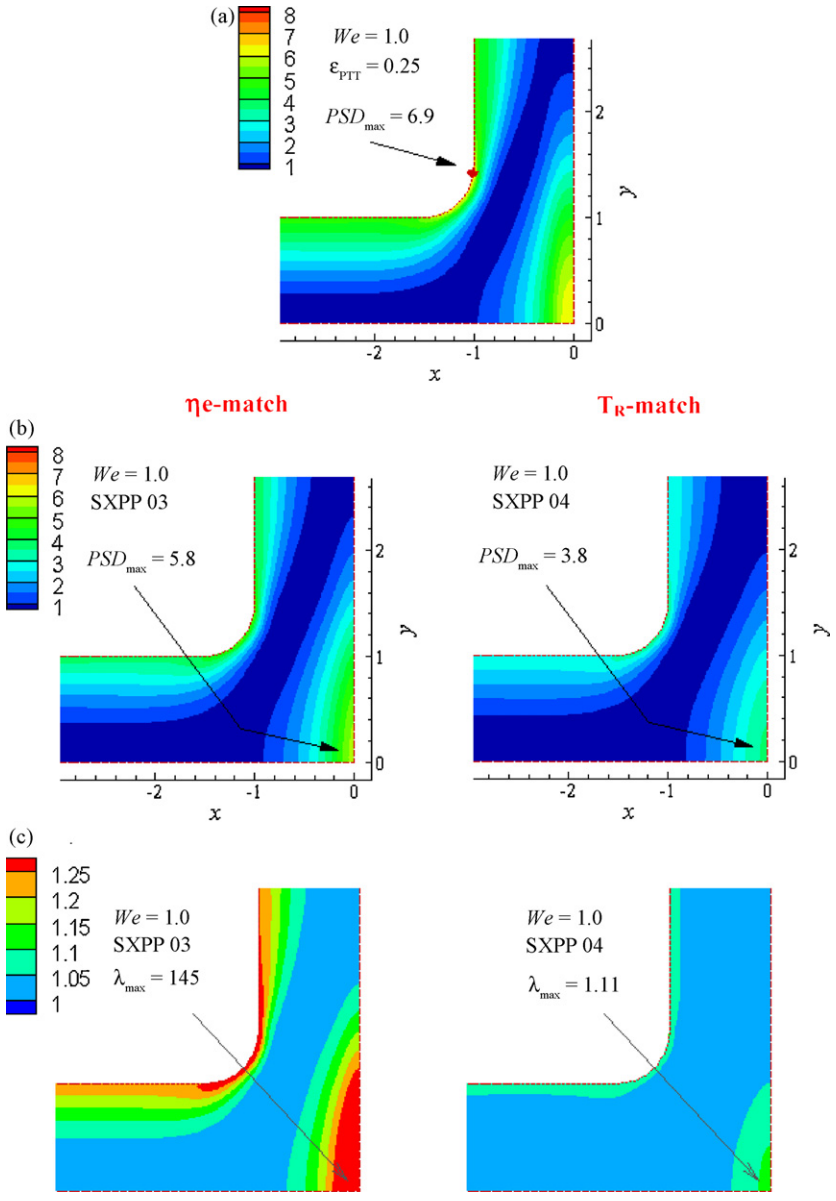

Fig. 23. *PSD* patterns of (a) e-PTT with $\varepsilon_{PTT} = 0.25$ and its corresponding (b) SXPP model matching and (c) backbone-stretch fields.

$O(10\,\mathrm{U})$ for SXPP-fluid 2. In addition, shear-thinning is even more prominent under SXPP-fluid 2, with onset around a decade earlier than for SXPP-fluid 1, this being reflected through more significant departure from the e-PTT fluid 1 thinning behaviour.

The *PSD* contour patterns at $We = 1$ are provided in Fig. 21 for the e-PTT fluid offering comparison against those for SXPP-fluid 1 and SXPP-fluid 2. These *PSD* patterns may be interpreted across the various regions of flow through the corresponding shear and extensional viscometric plots of Fig. 20. The general summary is that the markedly similar *PSD* patterns are established for SXPP-fluid 1 in contrast to e-PTT fluid 1, with greater departure noted from the patterns for SXPP-fluid 2. On the symmetry-line, this can be explained via the closer extensional viscosity response of SXPP-fluid 1 to that for e-PTT fluid 1, and as distinct from that for SXPP-fluid 2, specifically in the deformation rate region where $\dot{\varepsilon} < 1.4$ (the regime below the predicted Newtonian field maximum strain-rate). The uniformly larger η_e-response for SXPP-fluid 1 over fluid 2, leads to sustained N_1-levels beyond the stagnation point, which are even more strongly reinforced under the e-PTT option (strong extensional outflow response). Hence, similar levels of N_1-maxima are extracted with SXPP-fluid 1 and e-PTT fluid 1 of 12.7 and 20.7 U ($O(10–20)$), respectively. As anticipated, N_1-maxima with SXPP-fluid 2 stand at the level of one-third of e-PTT fluid 1, and these remain a local feature to the stagnation point region. The position and response in shear flow is exposed by the region along the wall and at the bend (so, a reflection of T_{xy}-levels). Typically at $\dot{\gamma} = 2$ units, the e-PTT fluid 1 has the highest level of shear viscosity, followed by SXPP fluid 1, and then SXPP fluid 2, respectively. The results are entirely consistent with this description, once again demonstrating the closer proximity in wall shear stress distributions between SXPP-fluid 1 and e-PTT fluid 1, with more strongly sustained levels travelling along the wall towards the outflow in the case of the e-PTT fluid (less thinning). In comparison, the wall shear stress distribution for SXPP-fluid 2, remains relatively localised to the bend region alone. This would indicate that the wall shear-rate maxima at the bend region lie around $O(10)\,\mathrm{U}$ to generate such complex flow differences in the solution profiles ($\partial v/\partial x \approx 8\,\mathrm{U}$). The comparable molecular-stretch fields are provided in Fig. 21c. This demonstrates how the largest levels of stretch occur both in shear flow along the walls and in the downstream extension zone. The

axima occur near the stagnation point and are significantly larger r SXPP-fluid 1 over fluid 2. This position contrasts to findings for ntraction flows where maximum stretch tends to occur around e re-entrant corner and along the downstream wall boundary ver [28].

.2 Matching η_e and Tr on moderate-hardening/strain-softening PTT (ε_{PTT} = 0.25) and SXPP models

The viscometric properties for e-PTT fluid 2 with $\varepsilon = 0.25$, reflect ear-thinning behaviour and slight strain hardening prior to the wtonian maximum extension-rate, followed by the overriding ftening behaviour that occurs thereafter. Fig. 22 depicts the plot shear and extensional viscosities, inclusive of Trouton ratio, for PTT fluid 2 in contrast to SXPP-fluids 3 and 4 (material parameters also provided in Table 2). Once more, the strategy is to match either peak of extensional viscosity (SXPP-fluids 3) or Trouton ratio (SXPP-fluids 4). Of significant interest is the fact that e SXPP-fluid 4 has a distinctly lower extensional viscosity in the gime of $We\,\dot{\varepsilon} < 1.4$, when taken against that for e-PTT fluid 2 d SXPP-fluids 3. Here, η_e maxima is $O(4\,\mathrm{U})$ for e-PTT fluid 2, t with no sign of hardening with SXPP-fluids 3. This means that these two fluid options, the e-PTT fluid 2 displays the slightly ore dominant extensional viscosity behaviour up to $\dot{\varepsilon} < 2.5$, with vitchover beyond this point to that for SXPP-fluids 3. In Trouton ratio, the SXPP-fluids 3 is seen to dominate the e-PTT fluid 2 sponse even earlier, by $\dot{\varepsilon} > 0.5$, due to the additional contribution its premature and slightly more rapid shear-thinning behaviour. oving to consider SXPP-fluid 4 data, scaled *Tr* maxima of $O(2\,\mathrm{U})$ e gathered, with close proximity borne out between the relative behaviour of both SXPP-fluid 4 and e-PTT fluid 2 over a wide nge of deformation rates (note, maxima separated by one decade). t, this stimulates significant disparity in extensional viscosity sponse, from $O(2)$ for SXPP-fluid 4 (softening) to $O(4)\,\mathrm{U}$ for e-T fluid 2 (hardening) at the representativeNewtonian maximum tension-rate of $\dot{\varepsilon} = 1.4$. Such dominance persists up to $\dot{\varepsilon} < 30$. ere is only a slightly more exaggerated shear-thinning rate in PP-fluid 4 over its counterpart SXPP-fluids 3. This, and the softing extensional viscosity response, together lead to the overall ore moderate levels of Trouton ratio produced for SXPP-fluid 3 d 4 over those captured with SXPP-fluid 1 and 2 (maxima one der lower).

Generally, the *PSD* patterns as shown in Fig. 23 demonstrate e characteristic features linked with fluids of strain-softening haviour, where the levels of stress generated are considerably wer than those produced with their strain-hardening alternatives, discussed above. The correspondence in *PSD* patterns largely follows the trends associated with the extensional viscosity data, so at the *PSD* pattern for SXPP-fluid 3 assumes much closer agreement with e-PTT fluid 2 than does the pattern for SXPP-fluid 4. The proved matching is conveyed around the stagnation point zone the symmetry-line, and particularly in the local downstream gion beyond the stagnation point. As above, correspondingly simr levels of N_1-maxima generated confirm this position, through PP-fluid 3 and e-PTT fluid 2 of 4.2 and 5.7 U ($O(4)$, one order cline from that with strain-hardening versions), respectively. is lies in contrast to the N_1-maxima for the SXPP-fluid 4 of $O(2)\,\mathrm{U}$, trictly localised feature to the stagnation point region. The shear ess behaviour, represented at the bend region in *PSD* contour ucture, takes up form more similar between SXPP-fluid 3 and PTT fluid 2, being close to that extracted for the SXPP-fluid 2. is is in-line with the shear viscosity functionality, specifically ound deformation rates $O(1)$. Such trends indicate a maximum stained around the bend that provides relatively localised distritions thereabouts. In contrast to the *PSD* patterns for SXPP-fluid the trend with SXPP-fluid 4 is to damp such wall-shear stress axima and concentrate the distribution around the bend region. This would imply deformation rates are achieved locally between $O(1)$ and $O(10)\,\mathrm{U}$ (actually $O(8)\,\mathrm{U}$). The relative field position for molecular backbone-stretch is also included in Fig. 23c. Similar comments apply here as with PSD-data (see Fig. 21c). For SXPP-fluid 3, the backbone-stretch distribution is a scaled-down from of that for SXPP-fluid 2, with $\lambda_{max} = 1.45$ at the stagnation zone. The stretch field for SXPP-fluid 4 is significantly suppressed in comparison, reflecting only 10% increase above the unstretched state at maximum.

4. Conclusions

In this paper, the numerical computation of steady-state viscoelastic flow in cross-slot device has been analysed, through various choices of constitutive model, problem setting and finite element/finite volume pressure-correction implementations. As anticipated, the flow along the symmetry line of the cross-slot is found to behave as in planar elongation (constrained by incompressibility), whilst shear behaviour is observed on the walls of the cross-slot device, with a mixture of shear and extensional flow elsewhere. Often, the critical state of elasticity in a general flow may be linked to the singularity in the extensional viscosity, particularly for severe strain-hardening fluids, as with the Oldroyd-B model. It is conspicuous that, such a critical state not only depends on the presence of this singularity, but also upon the rate of rise in the extensional viscosity (i.e. normal stress difference in extension). This has been gathered from L-PTT solutions with $\varepsilon \leq 10^{-3}$, where the singularity in extensional viscosity has been removed, yet the critical state remains as for the unbounded Oldroyd-B model (at $We = 0.35$). Beyond this elasticity level, numerical solutions tend towards a pseudo-steady state, and flow fields are found to depend upon the precise form of stress discretisation, in and around the neighbourhood of the solution singularity at the stagnation point. In general, the presence of the convective stress term in the momentum equation for a polymeric fluid has shifted the normal stress and *PSD* profiles downstream towards the outflow, whilst increasing the strain-rate level on the symmetry line.

Cross-slot flow solutions for a Newtonian model reveal symmetrical trends in all flow fields, a reflection of the lack of memory effects. In creeping flow, the maximum strain-rate of $\sim$1.4 U occurs at the stagnation point, being about triple that observed in a 4:1 planar contraction flow. This numerical value of strain-rate can be utilised in the prediction of the critical elasticity state for an Oldroyd-B viscoelastic fluid, where the maximum strain-rate in the shear-free zone is less than for the equivalent Newtonian fluid. The ellipsoidal cat's eye structure, characterised by a zero-*PSD* level, is clearly apparent around the bend of the flow domain. Inertial influence ($0 \leq Re \leq 60$) has a direct effect on lowering the maximum level of *PSD* without significantly disturbing the symmetrical form of its symmetry-line profile. However, one may note that the cat's eye shape is more elongated towards the inflow as inertia increases.

The approximate critical state for the Oldroyd-B fluid model is at $We = 0.35$. Beyond this level of elasticity, steady-state numerical solutions tend to a *pseudo steady state*, for which flow fields are dependent on the particular stress treatment in each algorithm. For the more solvent-dominated fluid ($\beta = 0.9$), the deformation rate peak-level is practically unaffected by rise in elasticity. Alternatively, for the more polymeric-based fluid (smaller β value), the peak-level is reduced with increasing elasticity, accompanied by a rising trend in the downstream tail of the profile. As We_{crit} is approached, oscillations occur in extension-rate at the peak around the stagnation point, being larger in amplitude and frequency for the more polymeric-based fluids, and being constrained for the more solvent-based materials. Oscillations become larger with increasing elasticity, particularly for $\beta = 1/9$ (as noted in extension-

rate, see Fig. 11). For $\beta = 0.9$, these oscillations are only apparent at relatively elevated levels of *We*, when *We* = 0.5.

Matching rheology between any two rheological models may be performed so that the two fluids have the closest rheometric behaviour in the dynamic range of interest for a specific problem. For example in these cross-slot flows, successful attempts have been made to match rheological response and observe solutions through *PSD* fields, between strain-hardening polymeric Oldroyd-B and constant shear viscosity FENE-CR models. This applies up to an elasticity level of *We* = 0.5 and via a suitable selection of their respective material parameters/functions. Similarly, strain hardening and strain softening e-PTT (network-based) models have been rheologically matched to SXPP (kinetic-based) models. Equitable trends in solution response (in complex deformation) through *PSD* behaviour are found when matching on the extensional viscosity in contrast to the Trouton ratio. From *PSD*-fields, N_1-maxima on the flow symmetry line and T_{xy}-maxima along the wall and around the bend together map out this correspondence. The SXPP fluid solutions also provide further detail on field distribution of the molecular backbone-stretch. This is most emphatically demonstrated in the severe strain-hardening mode, with extrema in shear flow at the walls and in the downstream extension zone (latter dominant).

Here, the viscoelastic flow in cross-slot devices has been demonstrated as an effective tool to study the rheological properties of viscoelastic fluids, notably within the present context of planar elongation. This comes from the symmetrical form of the flow domain and the relatively large value of the strain-rates generated (long particle dwelling times). From viscometric data and numerical solutions, derivation of local peaks in deformation rate has lead to the accurate prediction of maximum levels of normal stress for some models. This can provide a key to aid the careful selection of appropriate constitutive model with suitable material functions, so that predictions can elucidate quantitative agreement with experimental findings.

Acknowledgements

The authors gratefully acknowledge financial support under the EPSRC grant 'Complex Fluids and Complex Flows - Portfolio Partnership'. Authors are also grateful for helpful discussions with Prof. Malcom Mackley (Cambridge University) on this topic. BP acknowledges the financial support of the government of Thailand.

Appendix A. Shear and extensional viscosity equations for various material models

It this appendix, we provide the necessary formulation employed with regard to the different models introduced in the present study. In this respect, various constitutive equations and expression of shear and elongational viscosities, respectively, are explicitly presented.

The general form for the constitutive equation (of type) may be re-written as

$$\frac{\partial \boldsymbol{\tau}}{\partial t} = -\mathbf{u}\cdot\nabla\boldsymbol{\tau} + 2\frac{\mu_p}{We}\boldsymbol{D} + \left(\nabla\mathbf{u}\cdot\boldsymbol{\tau} + \boldsymbol{\tau}.\nabla\mathbf{u}^T\right) - \frac{\mathbf{f}_{We}^{\text{model}}(\boldsymbol{\tau})}{We} - \mathbf{f}_{\boldsymbol{\tau D}}^{\text{model}}(\boldsymbol{\tau},\boldsymbol{D}).$$

For example, for an Oldroyd-B model, the constitutive equation is retrieved for:

$$\mathbf{f}_{We}^{Old}(\boldsymbol{\tau}) = \boldsymbol{\tau}; \quad \mathbf{f}_{\boldsymbol{\tau}D}^{Old} = 0,$$

this leads to expressions for the shear and elongational viscosity of:

$$\eta_s = \mu_s + \mu_p; \quad \eta_e = 4\mu_s + \frac{2\mu_p}{1-2\,We\,\dot{\varepsilon}} + \frac{2\mu_p}{1+2\,We\,\dot{\varepsilon}}.$$

Similarly, for the linear and exponential PTT model, functions are set, respectively, as

$$\mathbf{f}_{We}^{LPTT}(\boldsymbol{\tau}) = f(\boldsymbol{\tau})\,\boldsymbol{\tau} = \left(1 + \varepsilon_{PTT}\frac{We}{\mu_p}tr(\boldsymbol{\tau})\right)\boldsymbol{\tau}; \quad \text{or}$$

$$\mathbf{f}_{We}^{ePTT}(\boldsymbol{\tau}) = e^{(\varepsilon_{PTT}(We/\mu_p)tr(\boldsymbol{\tau}))}\boldsymbol{\tau}; \quad \mathbf{f}_{\boldsymbol{\tau}D}^{PTT} = \xi(\boldsymbol{\tau}\cdot\boldsymbol{D} + \boldsymbol{D}\cdot\boldsymbol{\tau}).$$

Thus, shear and extensional viscosity are:

$$\eta_s = \mu_s + \frac{f\mu_p}{f_{L/ePTT}^2 - \dot{\gamma}^2 We^2\xi\left(\xi-2\right)};$$

$$\eta_e = 4\mu_s + \frac{2\mu_p}{f_{PTT} - 2We\dot{\varepsilon}(1-\xi)} + \frac{2\mu_p}{f_{PTT} + 2We\dot{\varepsilon}\left(1-\xi\right)}.$$

For the single XPP model, the following functions are employed in the constitutive equation:

$$\mathbf{f}_{We}^{SPP}(\boldsymbol{\tau}) = F(\Lambda,\boldsymbol{\tau})\boldsymbol{\tau} + \frac{\mu_p}{We}\left[F(\Lambda,\boldsymbol{\tau}) - 1\right]\mathbf{I} + \alpha\frac{We}{\mu_p}\boldsymbol{\tau}\cdot\boldsymbol{\tau}; \quad \mathbf{f}_{\boldsymbol{\tau}D}^{XPP}(\boldsymbol{\tau},\boldsymbol{D}) = 0,$$

where

$$F(\Lambda,\tau) = \frac{2}{\varepsilon}\left(1-\frac{1}{\Lambda}\right)e^{(2/q)(\Lambda-1)} + \frac{1}{\Lambda^2}\left(1 - \left(\frac{We}{\mu_p}\right)^2\frac{\alpha}{3}tr(\boldsymbol{\tau}\cdot\boldsymbol{\tau})\right),$$

with

$$\Lambda = \sqrt{1 + \frac{1}{3}\frac{We}{\mu_p}tr(\boldsymbol{\tau})}; \quad \varepsilon = \frac{\lambda_{0s}}{\lambda_{0b}}; \quad We = \lambda_{0b}\frac{U}{L},$$

and

$$\mathbf{f}_{We}^{SPP}(\boldsymbol{\tau}) = \begin{pmatrix} f_{xx}\boldsymbol{\tau}_{xx} & f_{xy}\boldsymbol{\tau}_{xy} & 0 \\ f_{xy}\boldsymbol{\tau}_{xy} & f_{yy}\boldsymbol{\tau}_{yy} & 0 \\ 0 & 0 & f_{zz}\boldsymbol{\tau}_{zz} \end{pmatrix}.$$

This realises shear and elongational viscosities of:

$$\eta_s = \mu_s + \frac{\mu_p}{f_{xy}}; \quad \eta_e = 4\mu_s + \frac{2\mu_p}{f_{yy} - 2We\dot{\varepsilon}(1-\xi)} + \frac{2\mu_p}{f_{xx} + 2We\dot{\varepsilon}(1-\xi)}.$$

For a FENE-CR model, the stress is expressed through a conformation transformation as

$$\boldsymbol{\tau} = \frac{\mu_p}{\lambda}f(\mathbf{A})(\mathbf{A}-\mathbf{I}),$$

where

$$\frac{\partial \mathbf{A}}{\partial t} = -\mathbf{u}\cdot\nabla\mathbf{A} + (\nabla\mathbf{u}\cdot\mathbf{A} + \mathbf{A}.\nabla\mathbf{u}^T) - \frac{\mathbf{f}_{We}^{FENE}(\mathbf{A})}{We} - \mathbf{f}_{\mathbf{AD}}^{FENE}(\mathbf{A},\boldsymbol{D}),$$

with the following functions used in the constitutive equation:

$$\mathbf{f}_{We}^{FENE} = f(\mathbf{A})(\mathbf{A}-\mathbf{I}), \quad f(\mathbf{A}) = \frac{1}{1 - tr(\mathbf{A})/L^2}; \quad \mathbf{f}_{\mathbf{AD}}^{FENE} = 0,$$

and

$$\eta_s = \mu_s + \mu_p; \quad \eta_e = 4\left(\mu_s + \frac{f_{FENE}\mu_p}{(f_{FENE} - 2\dot{\varepsilon}We)(f_{FENE} + 2\dot{\varepsilon}We)}\right).$$

ferences

] C.W. Macosko, Rheology: Principles, Measurements, and Applications, VCH Publisher Inc., New York, 1994.
] F.A. Morrison, Understanding Rheology, Oxford University Press Inc., New York, 2001.
] T. Sridhar, V. Tirtaatmadja, D.A. Nguyen, R.K. Gupta, Measurement of extensional viscosity of polymer-solutions, J. Non-Newtonian Fluid Mech. 40 (1991) 271–280.
] J. Meissner, Development of a universal extensional rheometer for uniaxial extension of polymer melts, J. Rheol. 16 (1972) 405–420.
] J. Meissner, J. Hostettler, A new elongational rheometer for polymer melts and other highly viscoelastic liquids, Rheol. Acta 33 (1994) 1–21.
] J. Meissner, T. Raible, S.E. Stephenson, Rotary clamp in uniaxial and biaxial extensional rheometry of polymer melts, J. Rheol. 25 (1981) 1–28.
] S. Chatraei, C.W. Macosko, H.H. Winter, Lubricated squeezing flow—a new biaxial extensional rheometer, J. Rheol. 25 (1981) 433–443.
] D.M. Binding, An approximate analysis for contraction and converging flows, J. Non-Newtonian Fluid Mech. 27 (1988) 173–189.
] F.N. Cogswell, Converging flow of polymer melts in extrusion dies, Polym. Eng. Sci. 12 (1972) 64–73.
] J.F.M. Schoonen, F.H.M. Swartjes, G.W.M. Peters, F.P.T. Baaijens, H.E.H. Meijer, A 3D numerical/experimental study on a stagnation flow of a polyisobutylene solution, J. Non-Newtonian Fluid Mech. 79 (1998) 529–561.
] W.M.H. Verbeeten, G.W.M. Peters, F.P.T. Baaijens, Viscoelastic analysis of complex polymer melt flows using the eXtended Pom-Pom model, J. Non-Newtonian Fluid Mech. 108 (2002) 301–326.
] K.D. Coventry, M.R. Mackley, Cross-slot extensional flow birefringence observations of polymer melts using a multi-pass rheometer, J. Rheol. 52 (2008) 401–415.
] J.F.M. Schoonen, Determination of rheological constitutive equations using complex flows, Ph.D. Thesis, Technische Universiteit Eindhoven (1998).
] A.C.B. Bogaerds, W.M.H. Verbeeten, G.W.M. Peters, F.P.T. Baaijens, 3D viscoelastic analysis of a polymer solution in a complex flow, Comput. Methods Appl. Mech. Eng. 180 (1999) 413–430.
] J. Remmelgas, P. Singh, L.G. Leal, Computational studies of nonlinear elastic dumbbell models of Boger fluids in a cross-slot flow, J. Non-Newtonian Fluid Mech. 88 (1999) 31–61.
] P. Singh, L.G. Leal, Finite-element simulation of flow around a 3-Pi/2 corner using the FENE dumbbell model, J. Non-Newtonian Fluid Mech. 58 (1995) 279–313.
] W.M.H. Verbeeten, Computational polymer melt rheology, Ph.D. Thesis, Technische Universiteit Eindhoven (2001).
] M.R. Mackley, R.T.J. Marshall, J.B.A.F. Smeulders, The multipass rheometer, J. Rheol. 39 (1995) 1293–1309.
] G.N. Rocha, R.J. Poole, M.A. Alves, P.J. Oliveira, On extensibility effects in the cross-slot flow bifurcation, J. Non-Newtonian Fluid Mech. 156 (2009) 58–69.
] S.-S. Hsieh, C.-H. Liu, J.-H. Liou, Dynamics of DNA molecules in a cross-slot microchannel, Meas. Sci. Technol. 18 (2007) 2907–2915.
] D.G. Crowley, F.C. Frank, M.R. Mackley, R.G. Stephenson, Localized flow birefringence of polyethylene oxide solutions in a 4 roll mill, J. Polymer Sci. A2 14 (1976) 1121–1131.
] F.T. Trouton, On the coefficient of viscous traction and its relation to that of viscosity, in: Proceedings of the Royal Society of London, Series A, Containing Papers of a Mathematical and Physical Character (1905–1934), vol. 77, 1906, pp. 426–440.
[23] N. Clemeur, R.P.G. Rutgers, B. Debbaut, Numerical evaluation of three dimensional effects in planar flow birefringence, J. Non-Newtonian Fluid Mech. 123 (2004) 105–120.
[24] P. Wapperom, M.F. Webster, Simulation for viscoelastic flow by a finite volume/element method, Comput. Methods Appl. Mech. Eng. 180 (1999) 281–304.
[25] M.F. Webster, H.R. Tamaddon-Jahromi, M. Aboubacar, Time-dependent algorithm for viscoelastic flow-finite element/volume schemes, Numer. Methods Part. Diff. Eqns. 21 (2005) 272–296.
[26] F. Belblidia, I.J. Keshtiban, M.F. Webster, Stabilised computations for viscoelastic flows under compressible implementations, J. Non-Newtonian Fluid Mech. 134 (2006) 56–76.
[27] F. Belblidia, H. Matallah, B. Puangkird, M.F. Webster, Alternative subcell discretisations for viscoelastic flow: stress interpolation, J. Non-Newtonian Fluid Mech. 146 (2007) 59–78.
[28] I.J. Keshtiban, B. Puangkird, H. Tamaddon-Jahromi, M.F. Webster, Generalised approach for transient computation of start-up pressure-driven viscoelastic flow, J. Non-Newtonian Fluid Mech. 151 (2008) 2–20.
[29] K. Walters, M.F. Webster, The distinctive CFD challenges of computational rheology, Int. J. Numer. Method Fluids 43 (2003) 577–596.
[30] J.P. Aguayo, H.R. Tamaddon-Jahromi, M.F. Webster, Extensional response of the pom-pom model through planar contraction flows for branched polymer melts, J. Non-Newtonian Fluid Mech. 134 (2006) 105–126.
[31] J.L. Guermond, L. Quartapelle, On stability and convergence of projection methods based on pressure Poisson equation, Int. J. Numer. Method Fluids 26 (1998) 1039–1054.
[32] E.O.A. Carew, P. Townsend, M.F. Webster, A Taylor–Petrov–Galerkin algorithm for viscoelastic flow, J. Non-Newtonian Fluid Mech. 50 (1993) 253–287.
[33] F. Belblidia, H. Matallah, M.F. Webster, Alternative subcell discretisations for viscoelastic flow: velocity gradient approximation, J. Non-Newtonian Fluid Mech. 151 (2008) 69–88.
[34] M.F. Webster, H. Matallah, K.S. Sujatha, Sub-cell approximations for viscoelastic flows—filament stretching, J. Non-Newtonian Fluid Mech. 126 (2005) 187–205.
[35] H. Matallah, P. Townsend, M.F. Webster, Recovery and stress-splitting schemes for viscoelastic flows, J. Non-Newtonian Fluid Mech. 75 (1998) 139–166.
[36] N.D. Waters, M.J. King, Unsteady flow of an elastico-viscous liquid, Rheol. Acta 9 (1970) 345–355.
[37] M. Aboubacar, H. Matallah, M.F. Webster, Highly elastic solutions for Oldroyd-B and Phan-Thien/Tanner fluids with a finite volume/element method: planar contraction flows, J. Non-Newtonian Fluid Mech. 103 (2002) 65–103.
[38] M. Aboubacar, H. Matallah, H.R. Tamaddon-Jahromi, M.F. Webster, Numerical prediction of extensional flows in contraction geometries: hybrid finite volume/element method, J. Non-Newtonian Fluid Mech. 104 (2002) 125–164.
[39] R.J. Poole, M.A. Alves, P.J. Oliveira, Purely elastic flow asymmetries, Phys. Rev. Lett. 99 (2007) 164503–164504.
[40] K.D. Coventry, Cross-slot rheology of polymers, Ph.D. Thesis, University of Cambridge, Department of Chemical Engineering (2006).
[41] N. Clemeur, R.P.G. Rutgers, B. Debbaut, On the evaluation of some differential formulations for the pom-pom constitutive model, Rheol. Acta 42 (2003) 217–231.